

# Electrodynamics of Outer-Gap Accelerator: Formation of Soft Power-law Spectrum Between 100 MeV and 3 GeV

Kouichi Hirotani, Alice K. Harding

*Code 661.0, Laboratory for High Energy Astrophysics,  
NASA/Goddard Space Flight Center, Greenbelt, MD 20771;  
hirotani@milkway.gsfc.nasa.gov, Alice.K.Harding@nasa.gov*

and

Shinpei Shibata

*Department of Physics, Yamagata University, Yamagata 990-8560, Japan;  
shibata@sci.kj.yamagata-u.ac.jp*

## ABSTRACT

We investigate a stationary pair production cascade in the outer magnetosphere of a spinning neutron star. The charge depletion due to global flows of charged particles, causes a large electric field along the magnetic field lines. Migratory electrons and/or positrons are accelerated by this field to radiate gamma-rays via synchro-curvature and inverse-Compton processes. Some of such gamma-rays collide with the X-rays to materialize as pairs in the gap. The replenished charges partially screen the electric field, which is self-consistently solved together with the distribution functions of particles and gamma-rays. By solving the set of Maxwell and Boltzmann equations, we demonstrate that an external injection of charged particles at nearly Goldreich-Julian rate does not quench the gap but shifts its position and that the particle energy distribution cannot be described by a power-law. The injected particles are accelerated in the gap and escape from it with large Lorentz factors. We show that such escaping particles migrating outside of the gap contribute significantly to the gamma-ray luminosity for young pulsars and that the soft gamma-ray spectrum between 100 MeV and 3 GeV observed for the Vela pulsar can be explained by this component. We also discuss that the luminosity of the gamma-rays emitted by the escaping particles is naturally proportional to the square root of the spin-down luminosity.

*Subject headings:* gamma-rays: observations – gamma-rays: theory – magnetic fields – methods: numerical – pulsars: individual (Geminga pulsar, PSR B1055-52, PSR B1706-44, Vela pulsar)

## 1. Introduction

Recent years have seen a renewal of interest in the theory of particle acceleration in pulsar magnetospheres, after the launch of the *Compton Gamma-ray Observatory* (e.g., for the Vela pulsar, Kanbach et al. 1994, Fierro et al. 1998; for PSR B1706–44, Thompson et al. 1996; for Geminga, Mayer-Hasselwander et al. 1994, Fierro et al. 1998; for PSR B1055–52, Thompson et al. 1999). The modulation of the  $\gamma$ -ray light curves testifies to the particle acceleration either at the polar cap (Harding, Tademaru, & Esposito 1978; Daugherty & Harding 1982, 1996; Sturner, Dermer, & Michel 1995), or at the vacuum gaps in the outer magnetosphere (Cheng, Ho, & Ruderman 1986a,b, hereafter CHR; Chiang & Romani 1992, 1994; Romani and Yadigaroglu 1995; Higgins & Henriksen 1997, 1998). Both models predict that electrons and positrons are accelerated in a charge depletion region, a potential gap, by the electric field along the magnetic field lines to radiate high-energy  $\gamma$ -rays via the curvature process. However, there is an important difference between these two models: An polar-gap accelerator releases very little angular momenta, while an outer-gap one could radiate them efficiently. In addition, three-dimensional outer-gap models commonly explain double-peak light curves with strong bridges observed for  $\gamma$ -ray pulsars. On these grounds, the purpose of the present paper is to explore further into the analysis of the outer-gap accelerator.

In the CHR picture, the gap is assumed to be geometrically thin in the transfield direction on the poloidal plane in the sense  $D_{\perp} \ll W$ , where  $D_{\perp}$  represents the typical transfield thickness of the gap, while  $W$  does the width along the magnetic field lines. In this limit, the acceleration electric field is partially screened by the zero-potential walls separated with a small distance  $D_{\perp}$ ; as a result, the gap, which is assumed to be vacuum, extends from the null surface to (the vicinity of) the light cylinder. Here, the null surface is defined as the place on which the local Goldreich-Julian charge density

$$\rho_{\text{GJ}} \equiv -\frac{\Omega B_z(s, z)}{2\pi c} \quad (1)$$

vanishes, where  $\Omega$  refers to the angular frequency of the neutron star,  $B_z$  the magnetic field component projected along the rotational axis, and  $c$  the velocity of light;  $(s, z)$  designates the position on the poloidal plane. If  $B_z > 0$  holds in the starward side of the null

surface, a positive acceleration field arises in the gap. The light cylinder is defined as the surface where the azimuthal velocity of a plasma would coincide with  $c$  if it corotated with the magnetosphere. Its radius from the rotational axis becomes the so-called ‘light cylinder radius’,

$$\varpi_{\text{LC}} \equiv \frac{c}{\Omega} \quad (2)$$

Particles are not allowed to migrate inwards beyond this surface because of the causality in special relativity.

It should be noted that the null surface is not a special place for the gap electrodynamics in the sense that the plasmas are not completely charge-separated in general and that the particles freely pass through this surface inwards and outwards. Therefore, the gap inner boundary is located near to the null surface, not because particle injection is impossible across this surface (as previously discussed), but because the gap is vacuum and transversely thin.

Then what occurs in the CHR picture if the gap becomes no longer vacuum? To consider this problem rigorously, we have to examine the Poisson equation for the electrostatic potential. In fact, as will be explicitly demonstrated in the next section, the original vacuum solution obtained in the pioneering work by Cheng et al. (1986) cannot be applied to a non-vacuum CHR picture. We are, therefore, motivated by the need to solve self-consistently the Poisson equation together with the Boltzmann equations for particles and  $\gamma$ -rays. Although the ultimate goal is to solve three-dimensional issues, a good place to start is to examine one-dimensional problems. In this context, Hirotani and Shibata (1999a, b, c; hereafter Papers I, II, III) first solve the Boltzmann equations together with the Maxwell equations one-dimensionally along the field lines, assuming that the gap is geometrically thick in the transfield direction in the sense  $D_{\perp} \gg W$ .

There is one important finding in this second picture: The gap position shifts if there is a particle injection across either of the boundaries (Hirotani & Shibata 2001, 2002a,b; hereafter Papers VII, VIII, IX). For example, when the injection rate across the outer (or inner) boundary becomes comparable to the typical Goldreich-Julian value, the gap is located close to the neutron star surface (or to the light cylinder). In other words, an outer gap is not quenched even when the injection rate of a completely charge-separated plasma across the boundaries approaches

the typical Goldreich-Julian value. Thus, an outer gap can coexist with a polar-cap accelerator; this forms a striking contrast to the first, CHR picture. It is also found in the second picture that an outer gap is quenched if the *created* particle density within the gap exceeds several percent of the Goldreich-Julian value. That is, the *discharge* of created pairs is essential to screen the acceleration field.

The purpose of this paper is to examine the second picture more closely. In all the previous works in the second picture, the particle energy distribution has been assumed to be mono-energetic in the sense that the particles attain the equilibrium Lorentz factor at each point, in a balance between the electrostatic acceleration and the radiation-reaction forces. In the present paper, we discard this assumption and explicitly consider the energy dependence of particles by solving the Boltzmann equations for positrons and electrons. We will demonstrate that the particle energy distribution cannot be represented either by a power law or by the mono-energetic approximation. We will further show that a power-law spectrum is generally formed in 100 MeV-GeV energies as a result of the superposition of the curvature spectra emitted by particles migrating at different positions.

In the next section, we describe the difficulties of electrodynamics found in the first picture. We then present the basic equations in § 3 and a numerical scheme to solve them in § 4. In § 5, we apply the theory to four  $\gamma$ -ray pulsars and compare the predictions with observations. In the final section, we discuss the possibilities of the unification of our picture with the CHR picture, as well as the unification of the outer-gap and polar-cap models.

## 2. Difficulties in Previous Outer-gap Models

To elucidate the electrodynamic difficulties in previous outer-gap models, let us examine the following Poisson equation for the electrostatic potential,  $\Psi$ :

$$-\frac{\partial^2 \Psi}{\partial s^2} - \frac{\partial^2 \Psi}{\partial z^2} = 4\pi[\rho_e(s, z) - \rho_{GJ}(s, z)], \quad (3)$$

where  $s$  and  $z$  refer to the coordinates parallel and perpendicular to the poloidal magnetic field, and  $\rho_e$  the true charge density. In the CHR picture,  $\rho_e$  grows exponentially in  $z$  direction, because the pair production rate at a specific altitude  $z$  is proportional to the integral of  $\rho_e$  over the altitude from the last-open field

line to  $z$ , namely

$$\rho_e \propto \int_0^z \rho_e(z') dz'. \quad (4)$$

Note that the  $\gamma$ -rays propagates only in the higher altitude direction, owing to the single-signed curvature of the magnetic field lines. Because of this exponential growth of  $\rho_e$ , it has been considered that most of the  $\gamma$ -rays are emitted from the higher altitudes in the gap. Moreover, to explain the observed  $\gamma$ -ray luminosities with a small  $D_\perp$ , one should assume that the created current density per magnetic flux tube with strength  $B$ , which is conserved along the field lines, becomes the typical Goldreich-Julian value,

$$\frac{c\rho_+}{B} + \frac{-c\rho_-}{B} \sim \frac{\Omega}{2\pi}, \quad (5)$$

where  $\rho_+$  (or  $\rho_-$ ) refers to the charge density of positrons (or electrons). At each point, we obtain  $\rho_e = \rho_+ + \rho_-$ . However, such a copious pair production will screen  $E_\parallel$  in higher altitudes in the gap, as the Poisson equation (3) indicates. This screening effect is particularly important near to the inner boundary, where we obtain  $\rho_e/B = \rho_-/B \sim -\Omega/(2\pi c)$  due to discharge. In the vicinity of the inner boundary, we can Fourier-analyze equation (3) in  $z$  direction to find out that the  $-\partial^2 \Psi / \partial z^2$  term contributes only to reduce  $\partial(-\partial\Psi/\partial s)/\partial s$ , that is, the  $s$  gradient of the acceleration field,  $-\partial\Psi/\partial s$ . Thus, a positive  $\rho_{GJ}$  must cancel the negative  $\rho_e$  to make the right-hand side be positive. That is, at the inner boundary,

$$-\frac{\rho_{GJ}}{B} = \frac{\Omega}{2\pi c} \frac{B_z}{B} > \frac{|\rho_e|}{B} \sim \frac{\Omega}{2\pi c} \quad (6)$$

must be satisfied. It follows that the polar cap, where  $B_z \sim B$  holds, is the only place for the inner boundary of the ‘outer’ gap to be located, if the created current in the gap is comparable to the typical Goldreich-Julian value (eq. [5]). Such a non-vacuum gap must extend from the polar cap (not from the null surface where  $\rho_{GJ}$  vanishes) to the light cylinder. We can therefore conclude that the original vacuum solution obtained by Cheng et al. (1986) cannot be applied to a non-vacuum CHR picture when there is a sufficient pair production that is needed to explain the observed  $\gamma$ -ray luminosity.

To construct a self-consistent model, we have to solve the Poisson equation for the electrostatic potential together with the Boltzmann equations for particles and  $\gamma$ -rays. We formulate them in the next section.

### 3. Basic Equations

#### 3.1. Poisson equation

Neglecting relativistic effects, and assuming that typical transfield thickness,  $D_{\perp}$ , is greater than or comparable to the longitudinal width,  $W$ , we can reduce the Poisson equation for non-corotational potential  $\Psi$  into the one-dimensional form (Hirotani 2000b, Paper VI; see also § 2 in Michel 1974)

$$-\nabla^2\Psi = -\frac{d^2\Psi}{ds^2} + \frac{\Psi}{D_{\perp}^2} = 4\pi \left[ \rho_e(s) + \frac{\Omega B_z(s)}{2\pi c} \right]. \quad (7)$$

As described at the end of § 3 in Paper VII, it is convenient to introduce the Debye scale length  $c/\omega_p$ , where

$$\omega_p = \sqrt{\frac{4\pi e^2}{m_e} \frac{\Omega B^{\text{in}}}{2\pi c e}}, \quad (8)$$

and  $B^{\text{in}}$  is the magnetic field strength at the inner boundary;  $e$  designates the magnitude of the charge on an electron,  $m_e$  the rest mass of an electron. Thus, we can introduce the following dimensionless coordinate variable:

$$\begin{aligned} \xi &\equiv \frac{\omega_p}{c} s \\ &= 1.87 \times 10^5 \Omega_2^{-1/2} \left( \frac{B^{\text{in}}}{10^5 \text{G}} \right)^{1/2} \left( \frac{s}{\varpi_{\text{LC}}} \right), \end{aligned} \quad (9)$$

where  $\Omega_2 \equiv \Omega/(10^2 \text{rad s}^{-1})$ .

By using such dimensionless quantities, we can rewrite the equation (7) into

$$E_{\parallel} = -\frac{d\psi}{d\xi} = -\frac{d\Psi}{ds} \cdot \frac{c}{\omega_p} \frac{e}{m_e c^2}, \quad (10)$$

$$\frac{dE_{\parallel}}{d\xi} = -\frac{\psi}{\Delta_{\perp}^2} + \frac{B(\xi)}{B^{\text{in}}} \left[ \int_1^{\infty} n_+ d\Gamma - \int_1^{\infty} n_- d\Gamma \right] + \frac{B_z(\xi)}{B^{\text{in}}} \quad (11)$$

where

$$\psi(\xi) \equiv \frac{e\Psi(s)}{m_e c^2}, \quad (12)$$

$$\Delta_{\perp} \equiv \frac{D_{\perp}}{c/\omega_p}, \quad (13)$$

and the particle distribution functions are defined by

$$n_{\pm}(\xi, \Gamma) \equiv \frac{2\pi c e}{\Omega} \frac{N_{\pm}(s, \Gamma)}{B(\xi)}; \quad (14)$$

$N_+(s, \Gamma)$  and  $N_-(s, \Gamma)$  represent the distribution functions of positrons and electrons, respectively, at position  $s$  and Lorentz factor  $\Gamma$ . We evaluate the dimensionless Goldreich-Julian charge density  $B_z/B^{\text{in}}$  in equation (11) at each  $s$ , by using the Newtonian dipole field (see eqs.[9]-[12] in Paper VIII for details).

#### 3.2. Particle Boltzmann Equations

On the poloidal plane, particles migrate along the magnetic field lines. Therefore, at time  $t$ , the distribution function  $N$  of particles obeys the following Boltzmann equation,

$$\frac{\partial N}{\partial t} + \frac{\mathbf{p}}{m_e \Gamma} \cdot \nabla N + \mathbf{F}_{\text{ext}} \cdot \frac{\partial N}{\partial \mathbf{p}} = S(t, s, \mathbf{p}), \quad (15)$$

where  $\mathbf{p}$  refers to the particle momentum,  $\mathbf{F}_{\text{ext}}$  the external forces acting on particles, and  $S$  the collisional terms. In the present paper,  $\mathbf{F}_{\text{ext}}$  consists of electrostatic acceleration and the synchro-curvature radiation reaction forces. Since the magnetic field is much less than the critical value ( $4.41 \times 10^{13}$  G), quantum effects can be neglected in the outer magnetosphere. As a result, synchro-curvature radiation takes place continuously and can be regarded as an external force acting on a particle. If we instead put the collisional term associated with the synchro-curvature process in the right-hand side, the energy transfer in each collision would be too small. We take the  $\gamma$ -ray production rate due to synchro-curvature process into account consistently in the  $\gamma$ -ray Boltzmann equations.

##### 3.2.1. Mono-pitch-angle Approximation

Let us briefly consider the pitch angle evolution of particles in the gap. Particles are created with initial Lorentz factors  $\Gamma_0 \sim 10^{3.5}$ , because the parent  $\gamma$ -ray photons have energies typically around GeV. For such ultra-relativistic particles, pitch angles do not evolve via synchro-curvature process, because the emission is beamed in the instantaneous velocities of the radiating particles. Instead, pitch angles decrease as the particles are accelerated along the field lines. Due to the curvature of magnetic field or the aberration of  $\gamma$ -rays, created particles will have initial pitch angles of a few tens of degrees. Thus, when particles are accelerated up to the Lorentz factor  $\Gamma$ , their pitch angles will be of the order of

$$\sin \chi = \frac{\Gamma_0}{\Gamma}, \quad (16)$$

where  $\Gamma_0 = 10^{3.5}$ . If IC scatterings contribute, or if the synchrotron process becomes important shortly after the creation (when  $\Gamma < 10^4$  holds), particles selectively lose transverse momenta and their pitch angles become less than the value in equation (16).

In the present paper, we assume that the pitch angles evolve as equation (16), evaluating  $\Gamma$  at the peak of  $n_{\pm}(\xi, \Gamma)$  in the momentum space. This treatment simplifies the problem significantly, because we can solve the particles' Boltzmann equation in the two-dimensional phase space  $(\xi, \Gamma)$ , rather than in the three-dimensional one  $(\xi, \Gamma, \chi)$ . Extension into the three-dimension phase space will be examined in our subsequent paper.

### 3.2.2. Stationary Boltzmann Equations

Utilizing the mono-pitch-angle approximation described just above, assuming that the distribution function does not change significantly during one gyration and that the toroidal magnetic field is negligibly small compared with the poloidal one, and imposing a stationary condition

$$\frac{\partial}{\partial t} + \Omega \frac{\partial}{\partial \phi} = 0, \quad (17)$$

we can reduce equation (15) to (Appendix A)

$$\frac{\partial n_+}{\partial \xi} + \left[ E_{\parallel} - \frac{P_{\text{SC}}(\xi, \Gamma)}{m_e c^2 \omega_p} \right] \frac{\partial n_+}{\partial \Gamma} = S_+(\xi, \Gamma), \quad (18)$$

$$\frac{\partial n_-}{\partial \xi} - \left[ E_{\parallel} - \frac{P_{\text{SC}}(\xi, \Gamma)}{m_e c^2 \omega_p} \right] \frac{\partial n_-}{\partial \Gamma} = S_-(\xi, \Gamma), \quad (19)$$

where  $\cos \chi = +1$  (or  $-1$ ) is used for positrons (or electrons). Radiation-reaction force due to synchro-curvature radiation,  $P_{\text{SC}}/c$ , is given by (Cheng et al. 2000)

$$\frac{P_{\text{SC}}}{c} = \frac{e^2 \Gamma^4 Q_2}{12 r_C} \left( 1 + \frac{7}{r_C^2 + Q_2^2} \right), \quad (20)$$

where

$$r_C \equiv \frac{c^2}{(r_B + \rho_c) (c \cos \chi / \rho_c)^2 + r_B \omega_B^2}, \quad (21)$$

$$\begin{aligned} Q_2^2 &\equiv \frac{1}{r_B} \left( \frac{r_B^2 + \rho_c r_B - 3 \rho_c^3}{\rho_c^3} \cos^4 \chi \right. \\ &\quad \left. + \frac{3}{\rho_c} \cos^2 \chi + \frac{1}{r_B} \sin^4 \chi \right); \end{aligned} \quad (22)$$

the radius and frequency of gyration are

$$r_B \equiv \frac{\Gamma m_e c^2 \sin \chi}{e B}, \quad (23)$$

$$\omega_B \equiv \frac{e B}{\Gamma m_e c}; \quad (24)$$

$\rho_c(s)$  refers to the radius of curvature. If we take the limit  $\chi \rightarrow 0$  or  $\pi$ ,  $P_{\text{SC}}$  reduces to a pure curvature radiation, which is proportional to  $\Gamma^4$ . On the other hand, if  $\rho_c \rightarrow \infty$ , it reduces to a pure synchrotron radiation, which is proportional to  $\Gamma^2$ .

If the magnetic field contains a significant toroidal component, azimuthal derivative terms appear in equations (18) and (19) due to the toroidal motion of the guiding center of gyrating particles. Nevertheless, the most important aspects of particle acceleration are expressed by these two equations. We thus adopt equations (18) and (19) as the particle Boltzmann equations. This treatment is justified in particular when the gap is located well inside of the light cylinder.

### 3.2.3. Collisional terms

We assume in this paper that  $\gamma$ -rays are either outwardly or inwardly propagating along the local magnetic field lines. For simplicity, we neglect the deviation of the  $\gamma$ -rays from the field lines due to magnetic curvature. Then the cosine of the collision angle  $\mu$  has a unique value  $\mu_+$  or  $\mu_-$ , corresponding to the  $\gamma$ -ray directions, provided that the soft photon field is unidirectional. In what follows, we assume that the soft photons are emitted from the neutron star and hence unidirectional at the gap. As a result,  $\mu_+$  and  $\mu_-$  are uniquely determined by the magnetic inclination  $\alpha_i$  and the position in the gap  $\xi$ . Under these assumptions, the source term can be expressed as

$$\begin{aligned} \omega_p S_+(\xi, \Gamma) &= - \int_{\epsilon_{\gamma} < \Gamma} d\epsilon_{\gamma} \eta_{\text{IC}}^{\gamma}(\epsilon_{\gamma}, \Gamma, \mu_+) n_+(\xi, \Gamma) \\ &\quad + \int_{\Gamma_i > \Gamma} d\Gamma_i \eta_{\text{IC}}^e(\Gamma_i, \Gamma, \mu_+) n_+(\xi, \Gamma_i) \\ &\quad + \frac{B^{\text{in}}}{B(\xi)} \int d\epsilon_{\gamma} \left[ \frac{\partial \eta_p(\epsilon_{\gamma}, \Gamma, \mu_+)}{\partial \Gamma} g_+ + \frac{\partial \eta_p(\epsilon_{\gamma}, \Gamma, \mu_-)}{\partial \Gamma} g_- \right] \end{aligned} \quad (25)$$

$$\omega_p S_-(\xi, \Gamma) = - \int_{\epsilon_{\gamma} < \Gamma} d\epsilon_{\gamma} \eta_{\text{IC}}^{\gamma}(\epsilon_{\gamma}, \Gamma, \mu_-) n_-(\xi, \Gamma)$$

$$+ \int_{\Gamma_i > \Gamma} d\Gamma_i \eta_{\text{IC}}^e(\Gamma_i, \Gamma, \mu_-) n_-(\xi, \Gamma_i) \\ + \frac{B^{\text{in}}}{B(\xi)} \int d\epsilon_\gamma \left[ \frac{\partial \eta_p(\epsilon_\gamma, \Gamma, \mu_+)}{\partial \Gamma} g_+ + \frac{\partial \eta_p(\epsilon_\gamma, \Gamma, \mu_-)}{\partial \Gamma} g_- \right] \quad (26)$$

where the dimensionless  $\gamma$ -ray distribution function  $g_\pm$  are defined as

$$g_\pm(\xi, \epsilon_\gamma) \equiv \frac{2\pi c e}{\Omega B^{\text{in}}} G_\pm(s, \epsilon_\gamma); \quad (27)$$

$G_\pm$  refers to the number of  $\gamma$ -rays per unit volume per unit dimensionless energy  $\epsilon_\gamma = h\nu_\gamma/m_e c^2$ . We will explicitly define the differential redistribution function for the pair production,  $\partial \eta_p/\partial \Gamma$ , by equation (39), after briefly describing the soft photon field in equations (31)-(38).

If we multiply  $d\Gamma$  on both sides of equation (25), or (26), the first (or the second) term in the right-hand side represents the rate of particles disappearing from (or appearing into) the energy interval  $m_e c^2 \Gamma$  and  $m_e c^2 (\Gamma + d\Gamma)$  due to inverse-Compton (IC) scatterings; the third (or the fourth) terms does the rate of particles created via collisions between the outgoing (or the ingoing)  $\gamma$ -rays and ambient soft photons. The positrons (or electrons) are supposed to collide with the soft photons at the same angle as the outwardly (or inwardly) propagating  $\gamma$ -rays; therefore, the same collision angle  $\cos^{-1} \mu_+$  (or  $\cos^{-1} \mu_-$ ) is used for both IC scatterings and pair production in equations (25) and (26). Since the pitch angles are very small (see eq. [16]), the difference of collision angles between  $e\gamma \rightarrow e\gamma$  and  $\gamma\gamma \rightarrow \gamma\gamma$  is negligible. The collisions tend to be head-on (or tail-on) for inwardly (or outwardly) propagating  $\gamma$ -rays, as the gap approaches the star.

The IC redistribution function  $\eta_{\text{IC}}^\gamma(\epsilon_\gamma, \Gamma, \mu)$  represents the probability that a particle with Lorentz factor  $\Gamma$  upscatters photons into energies between  $\epsilon_\gamma$  and  $\epsilon_\gamma + d\epsilon_\gamma$  per unit time when the collision angle is  $\cos^{-1} \mu$ . On the other hand,  $\eta_{\text{IC}}^e(\Gamma_i, \Gamma, \mu)$  describes the probability that a particle changes Lorentz factor from  $\Gamma_i$  to  $\Gamma$  in a scattering. Thus, energy conservation gives

$$\eta_{\text{IC}}^e(\Gamma_i, \Gamma_f, \mu) = \eta_{\text{IC}}^\gamma(\Gamma_i - \Gamma_f, \Gamma_i, \mu) \quad (28)$$

We introduce the following dimensionless IC redistribution functions,

$$\eta_{\text{IC}\pm,i}^\gamma(l) \equiv \frac{1}{\omega_p} \int_{b_{i-1}}^{b_i} \eta_{\text{IC}}^\gamma(\epsilon_\gamma, b_l, \mu_\pm) d\epsilon_\gamma, \quad (29)$$

where the particle Lorentz factor is  $\Gamma = b_l$ ; the  $\gamma$ -ray energy is divided into  $-l_0 + 1 + l_m = 15 + l_m$  bins as  $b_{l_0} = b_{-14} = 10^{-15/4} \times b_1$ ,  $b_{-13} = 10^{-14/4} \times b_1$ ,  $b_{-12} = 10^{-13/4} \times b_1, \dots, b_{-2} = 10^{-3/4} \times b_1$ ,  $b_{-1} = 10^{-2/4} \times b_1$ ,  $b_0 = 10^{-1/4} \times b_1$ ,  $b_1 = 10^5$ ,  $b_2 = b_1 + \Delta b, \dots, b_i = b_1 + (i-1)\Delta b, \dots, b_{l_m} = b_1 + (l_m-1)\Delta b$ . We normally use  $l_m = 256$  and  $\Delta b = 1.5 \times 10^5$ . In general,  $\eta_{\text{IC}\pm,i}^\gamma(l)$  can be defined by the soft photon flux  $dF_s/d\epsilon_s$  and the Klein-Nishina cross section  $\sigma_{\text{KN}}$  as follows:

$$\eta_{\text{IC}\pm,i}^\gamma(l) = \frac{1 - \beta \mu_\pm}{\omega_p} \\ \times \int_{\epsilon_{\text{min}}}^{\epsilon_{\text{max}}} d\epsilon_s \frac{dF_s}{d\epsilon_s} \int_{b_{i-1}}^{b_i} d\epsilon_\gamma \frac{d\epsilon_\gamma^*}{d\epsilon_\gamma} \int_{-1}^1 d\Omega_\gamma^* \frac{d\sigma_{\text{KN}}^*}{d\epsilon_\gamma^* d\Omega_\gamma^*} \quad (30)$$

where  $\beta \equiv \sqrt{1 - 1/\Gamma^2}$  is virtually unity,  $\Omega_\gamma$  the solid angle of upscattered photon, the asterisk denotes the quantities in the electron (or positron) rest frame. In the rest frame of a particle, a scattering always takes place well above the resonance energy. Thus, the classical formula of the Klein-Nishina cross section can be applied for the present problem. The soft photon flux per unit dimensionless photon energy  $\epsilon_s$  [ $s^{-1} \text{cm}^{-2}$ ] is written as  $dF_s/d\epsilon_s$ .

We assume in this paper that soft photons are supplied by the thermal radiation from the neutron star. If a soft emission component cannot be represented by a black body spectrum, we use the observed spectrum of  $dF_s/d\epsilon_s$  corrected for the interstellar absorption. If it can be represented by a blackbody component, we adopt

$$\frac{dF_s}{d\epsilon_s} = \pi \frac{B_s(T)}{\epsilon_s} \left( \frac{r_{\text{NS}}}{r} \right)^2, \quad (31)$$

where  $r$  and  $r_{\text{NS}}$  refers to the distance from the star center and the neutron star radius, respectively; the Planck function [ $\text{ergs s}^{-1} \text{cm}^{-2} \text{ster}^{-1} \text{ergs}^{-1}$ ] is related with the blackbody temperature ( $\delta \equiv kT/m_e c^2$ ) as

$$B_s(T) = \frac{2(m_e c^2)^3}{c^2 h^3} \frac{\epsilon_s^3}{\exp(\epsilon_s/\delta) - 1}. \quad (32)$$

Substituting equations (31) into (30), and executing the integration over  $\epsilon_\gamma$ , we obtain (Appendix B)

$$\eta_{\text{IC}\pm,i}^\gamma(l) = \frac{2\pi^2 e^4 m_e}{h^3 \omega_p} (1 - \beta \mu_\pm) \left( \frac{r_{\text{NS}}}{r} \right)^2 \\ \times \sum_j A_j \int_{\epsilon_{\text{min}}}^{\epsilon_{\text{max}}} d\epsilon_s \frac{\epsilon_s^2}{\exp(\epsilon_s/\delta_j) - 1} \int_{-1}^1 dx^* f_{\text{IC}}, \quad (33)$$

where

$$f_{\text{IC}} \equiv \begin{cases} z^2[z + 1/z + (x^*)^2 - 1], & \text{for } z_{i-1} < z < z_i \\ 0 & \text{otherwise;} \end{cases} \quad (34)$$

$$z \equiv \frac{1}{1 + \epsilon_s^*(1 - x^*)} \quad (35)$$

$$z_i \equiv \frac{b_i}{\Gamma(1 + \beta x^* \mu^*) \epsilon_s^*} = \frac{b_i}{b_l(1 + \beta x^* \mu^*) \epsilon_s^*} \quad (36)$$

$\mu^*$  and  $\epsilon_s^*$  are related with  $\mu$  and  $\epsilon_s$  by the Lorentz transformation as

$$\mu^* = \frac{\mu - \beta}{1 - \beta\mu}, \quad (37)$$

$$\epsilon_s^* = \Gamma(1 - \beta\mu)\epsilon_s. \quad (38)$$

Since  $\eta_{\text{IC}\pm,i}^*(l)$  is defined at  $\Gamma = b_l$ ,  $\Gamma$  is replaced with  $b_l$  in equation (36). Moreover,  $A_j$  is the observed emission area of the  $i$ th blackbody component normalized by  $4\pi r_{\text{NS}}^2$ . For example, if a soft photon field consists of the whole neutron star surface emission with temperature  $T_s$  and a heated polar cap emission with area  $\pi r_h^2$  and temperature  $T_h$ , we obtain  $A_1 = 1.0$ ,  $\delta_1 = kT_s/m_e c^2$  and  $A_2 = \pi r_h^2/(4\pi r_{\text{NS}}^2)$ ,  $\delta_2 = kT_h/m_e c^2$ .

To define a dimensionless pair-production redistribution function, we consider the case when a  $\gamma$ -ray photon with energy  $m_e c^2 b_l$  materializes as a pair with Lorentz factor  $b_l$ . Dividing the pair production rate [ $s^{-1}$ ] per Lorentz factor by  $\omega_p$ , we obtain

$$\begin{aligned} \eta_{p\pm,l}(i) &\equiv \frac{1}{\omega_p} \frac{\partial \eta_p}{\partial \Gamma}(b_i, b_l, \mu_\pm) \\ &= \frac{1 - \mu_\pm}{\omega_p} \int_{\epsilon_{\text{th}}}^\infty d\epsilon_s \frac{dF_s}{d\epsilon_s} \frac{d\sigma_p}{d\Gamma}, \end{aligned} \quad (39)$$

where the pair-production threshold energy is defined by

$$\epsilon_{\text{th}} \equiv \frac{2}{1 - \mu} \frac{1}{\epsilon_\gamma}. \quad (40)$$

The collision angles  $\cos^{-1} \mu_\pm$  are determined by the geometry, in the same manner as  $\eta_{\text{IC}\pm,i}^*$ . The differential cross section for pair production is given by

$$\begin{aligned} \frac{d\sigma_p}{d\Gamma} &= \frac{3}{8} \sigma_T \frac{1 - \beta_{\text{CM}}^2}{\epsilon_\gamma} \\ &\times \left[ \frac{1 + \beta_{\text{CM}}^2(2 - \mu_{\text{CM}}^2)}{1 - \beta_{\text{CM}}^2 \mu_{\text{CM}}^2} - \frac{2\beta_{\text{CM}}^4(1 - \mu_{\text{CM}}^2)^2}{(1 - \beta_{\text{CM}}^2 \mu_{\text{CM}}^2)^2} \right] \end{aligned} \quad (41)$$

where  $\sigma_T$  refers to the Thompson cross section and the center-of-mass quantities are defined as

$$\mu_{\text{CM}} \equiv \pm \frac{2\Gamma - \epsilon_\gamma}{\beta_{\text{CM}} \epsilon_\gamma}, \quad (42)$$

$$\beta_{\text{CM}}^2 \equiv 1 - \frac{1}{(1 - \mu)\epsilon_s \epsilon_\gamma}, \quad (43)$$

where  $\mu = \mu_+$  (or  $\mu_-$ ) for  $\eta_{p+,l}$  (or  $\eta_{p-,l}$ ).

Let us now discretize the differential equations. Denoting  $f_l^k$  as the quantity  $f$  evaluated at  $\xi = \xi^k$  and  $\Gamma = b_l$  (or  $\epsilon_\gamma = b_l$ ), the source terms (eq. [25] and [26]) can be represented as

$$\begin{aligned} S_{\pm,l}^k &= - \sum_{i < l} \eta_{\text{IC}\pm,i}^*(l) \cdot n_{\pm,l}^k + \sum_{i > l} \eta_{\text{IC}\pm,i}^*(i - l) n_{\pm,i}^k \\ &+ \frac{B^{\text{in}}}{B^k} \sum_i [\eta_{p+,l}(i) g_{+,i}^k + \eta_{p-,l}(i) g_{-,i}^k]. \end{aligned} \quad (44)$$

The dimensionless  $\gamma$ -ray distribution functions are defined above the energy  $m_e c^2 b_{l_0} = 5.11 \times 10^7$  eV as

$$g_{\pm,i}^k \equiv \frac{2\pi c e}{\Omega B^{\text{in}}} \int_{b_{i-1}}^{b_i} d\epsilon_\gamma G_\pm \left( \frac{c}{\omega_p} \xi^k, \epsilon_\gamma \right), \quad (45)$$

where  $i = l_0 + 1, \dots, -1, 0, 1, 2, \dots, l_m$ . On the other hand, the particle distribution functions are defined above  $\Gamma \geq b_1 = 10^5$  as

$$n_{\pm,i}^k \equiv \frac{2\pi c e}{\Omega B^k} N_\pm \left( \frac{c}{\omega_p} \xi^k, b_l \right), \quad (46)$$

where  $l = 1, 2, \dots, l_m$ . Note that  $n_\pm$  are normalized by  $B$  at each point  $\xi^k$ , while  $g_\pm$  are by  $B(\xi^{\text{in}})$ .

If we sum up the first and second terms in the right-hand side of equation (44) over  $l$ , the result vanishes identically. This is because the IC scatterings do not alter the particle number. Therefore,

$$\sum_l (S_{+l}^k - S_{-l}^k) = 0 \quad (47)$$

holds, because the created number of positrons is identical to that of electrons.

### 3.2.4. Current Conservation

Let us, for the moment, consider the current conservation problem. At each  $\xi$ , we are assuming that all the positrons (or electrons) have the same pitch angle  $\chi_+$  (or  $\chi_-$ ). In this case, the projected velocity along the poloidal magnetic field lines becomes

$c \sin \chi_+ \sqrt{1 - 1/\Gamma^2} \approx c \sin \chi_+$  for  $\Gamma \gg 1$ . It implies that particles at  $\xi = \xi^{k-1}$  migrate to  $\xi = \xi^k$  after time  $(\xi^k - \xi^{k-1})/(c \sin \chi_+)$ , irrespective of their Lorentz factor. Figure 1 shows this situation, describing the particle propagation along the characteristics, whose gradient is given by (see eq. 18)

$$\frac{d\Gamma}{d\xi} = E_{\parallel} - \frac{P_{\text{SC}}(\xi, \Gamma)}{m_e c^2 \omega_p} \quad (48)$$

in the phase space  $(\xi, \Gamma)$ . Adding the produced pairs between  $\xi^{k-1}$  and  $\xi^k$ , which are depicted by open circles in figure 1, we obtain

$$\sum_l n_{+,l}^k = \sum_l n_{+,l}^{k-1} + D^k \sum_l S_{+,l}^k \quad (49)$$

for positrons, where

$$D^k \equiv \xi^k - \xi^{k-1}. \quad (50)$$

Equation (49) holds even if IC scatterings, which do not change the total particle number, contribute. In the same manner, we obtain

$$\sum_l n_{-,l}^k = \sum_l n_{-,l}^{k-1} - D^k \sum_l S_{-,l}^k \quad (51)$$

for electrons. Adding both sides of these two equations, and utilizing equation (47), we obtain

$$\sum_l (n_{+,l}^k + n_{-,l}^k) = \sum_l (n_{+,l}^{k-1} + n_{-,l}^{k-1}). \quad (52)$$

On these grounds, we can conclude that the current density

$$j_{\text{tot}}^k \equiv \sum_l (n_{+,l}^k + n_{-,l}^k) \quad (53)$$

is virtually kept constant for  $k$  (i.e.,  $\xi = \xi^k$ ), provided  $\Gamma \gg \Gamma_0$ , which ensures  $\cos \chi_+ = +1$  (or  $-1$ ) for positrons (or electrons).

We solve the advection-type differential equations (18) and (19) on the two-dimensional phase space  $(\xi, \Gamma)$ , evaluating the source term by equation (44). The numerical method how to solve these partial differential equations will be described in § 4 in detail.

### 3.3. Gamma-ray Boltzmann Equations

In this subsection, we consider the  $\gamma$ -ray Boltzmann equations. For simplicity, we assume that the density of outwardly (or inwardly) propagating  $\gamma$ -rays decreases (or increases) at the same rate with the

magnetic field strength; this assumption gives a good estimate when  $W \ll \varpi_{\text{LC}}$  holds. Under this assumption, the  $\gamma$ -ray Boltzmann equations become (e.g., Paper VII)

$$\begin{aligned} \pm cB \frac{\partial}{\partial s} \left( \frac{G_{\pm}}{B} \right) &= - \int d\Gamma \frac{\partial \eta_p}{\partial \Gamma} \cdot G_{\pm}(s, \epsilon_{\gamma}) \\ &+ \int d\Gamma [\eta_{\text{IC}}^{\gamma}(\epsilon_{\gamma}, \Gamma, \mu_{\pm}) + \eta_{\text{SC}}(\epsilon_{\gamma}, \Gamma)] N_{\pm}(s, \Gamma), \end{aligned} \quad (54)$$

where  $\eta_{\text{SC}}$  is the synchro-curvature radiation rate [ $\text{s}^{-1}$ ] into the energy interval  $m_e c^2(\epsilon_{\gamma} + d\epsilon_{\gamma})$  by a particle migrating with Lorentz factor  $\Gamma$  (see Zhang & Cheng 1997 for the derivation and explicit expressions). The first term in the right-hand side expresses the  $\gamma$ -ray absorption rate by pair production, while the second term does the emission rate via IC scatterings and synchro-curvature radiation.

Integrating equations (54) over  $\epsilon_{\gamma}$  between  $b_{i-1}$  and  $b_i$ , we obtain

$$\begin{aligned} \left( \frac{dg_{\pm}}{d\xi} \right)_i &= \frac{d(\ln B)}{d\xi} g_{\pm,i} \mp \sum_l \eta_{p\pm,l}(b_i) \cdot g_{\pm,i} \\ &+ \sum_l [\eta_{\text{IC}\pm,i}^{\gamma}(l) + \eta_{\text{SC}\pm,i}(l)] n_{\pm}(\xi, b_i), \end{aligned} \quad (55)$$

where  $\eta_{\text{SC}+,i}(l)$  refers to the synchro-curvature radiation rate  $\eta_{\text{SC}}(b_i, b_l)$  by a positron having Lorentz factor  $\Gamma = b_l$ . In the same manner,  $\eta_{\text{SC}-,i}(l)$  does that by an electron.

Provided that the step size in  $\xi$  direction does not vary rapidly in the sense that  $|D^k - D^{k-1}| = O[(D^k)^2]$ , we can evaluate the left-hand side at  $\xi = \xi^{k-1}$  as

$$\left( \frac{dg_{\pm}}{d\xi} \right)_i^{k-1} = \frac{q^2 g_{\pm,i}^k + (1 - q^2) g_{\pm,i}^{k-1} - g_{\pm,i}^{k-2}}{q(1 + q) D^k} + O(D^2), \quad (56)$$

where  $q \equiv D^{k-1}/D^k$ .

Solving equation (56) for  $g_{\pm,i}^k$ , we obtain

$$g_{\pm,i}^k = \frac{q^2 - 1}{q^2} g_{\pm,i}^{k-1} + \frac{1}{q^2} g_{\pm,i}^{k-2} + q(q+1) D^k \left( \frac{dg_{\pm}}{d\xi} \right)_i^{k-1}. \quad (57)$$

In practice,  $q$  can deviates from 1.0, because the step size in  $\xi$  direction is free from the CFL condition (see § 4.2 for details). Therefore, even and odd steps affect each other in equation (57).

We evaluate the right-hand side of equation (55) at  $\xi = \xi^{k-1}$  and substitute the result into the last term of equation (57). Then we can solve the dimensionless  $\gamma$ -ray distribution function  $g_{\pm,i}^k$  in terms of the previous step values  $g_{\pm,i}^{k-1}$ ,  $g_{\pm,i}^{k-2}$ , and  $n_i^{k-1}$ .

### 3.4. Boundary Conditions

We now consider the boundary conditions to solve the set of Maxwell and Boltzmann equations (10), (11), (18), (19), and (57). At the *inner* (starward) boundary ( $\xi = \xi^{\text{in}}$ ), we impose (Paper VII)

$$E_{\parallel}(\xi^{\text{in}}) = 0, \quad (58)$$

$$\psi(\xi^{\text{in}}) = 0, \quad (59)$$

$$g_+^i(\xi^{\text{in}}) = 0 \quad (i = l_0 + 1, \dots, -1, 0, 1, 2, \dots, l_m), \quad (60)$$

$$n_{+,l}(\xi^{\text{in}}) = \begin{cases} j^{\text{in}}, & \text{for } l = 1 \\ 0, & \text{for } l = 2, 3, \dots, l_m \end{cases} \quad (61)$$

where the dimensionless positronic injection current across the inner boundary  $\xi = \xi^{\text{in}}$  is denoted as  $j^{\text{in}}$ . As we described at the end of § 3.2, current density is conserved along the magnetic flux tube if particles are accelerated well above the initial Lorentz factor. Thus, we obtain at  $\xi = \xi^{\text{in}}$

$$\sum_l n_{-,l}(\xi^{\text{in}}) = j_{\text{tot}} - j^{\text{in}}. \quad (62)$$

At the *outer* boundary ( $\xi = \xi^{\text{out}}$ ), we impose

$$E_{\parallel}(\xi^{\text{out}}) = 0, \quad (63)$$

$$g_-^i(\xi^{\text{out}}) = 0 \quad (i = l_0 + 1, \dots, -1, 0, 1, 2, \dots, l_m), \quad (64)$$

$$n_{-,l}(\xi^{\text{out}}) = \begin{cases} j^{\text{out}}, & \text{for } l = 1 \\ 0, & \text{for } l = 2, 3, \dots, l_m \end{cases} \quad (65)$$

The current density created in the gap per unit flux tube can be expressed as

$$j_{\text{gap}} = j_{\text{tot}} - j^{\text{in}} - j^{\text{out}}. \quad (66)$$

We adopt  $j_{\text{gap}}$ ,  $j^{\text{in}}$ , and  $j^{\text{out}}$  as the free parameters.

We have totally  $2l_m + 2(l_m - l_0 + 1) + 4$  boundary conditions (58)–(65) for  $2l_m + 2(l_m - l_0 + 1) + 2$  unknown functions  $n_{\pm,l}$ ,  $g_{\pm,i}$ ,  $\Psi$ , and  $E_{\parallel}$ . Thus two extra boundary conditions must be compensated by making the positions of the boundaries  $\xi^{\text{in}}$  and  $\xi^{\text{out}}$  be free. The two free boundaries appear because  $E_{\parallel} = 0$  is imposed at *both* the boundaries and because  $j_{\text{gap}}$  is

externally imposed. In other words, the gap boundaries ( $\xi^{\text{in}}$  and  $\xi^{\text{out}}$ ) shift, if  $j^{\text{in}}$  and/or  $j^{\text{out}}$  varies.

In practice, we give  $n_+(\xi^{\text{in}}, \Gamma)$  and  $n_-(\xi^{\text{in}}, \Gamma)$  by a continuous function of  $\Gamma$  near the lowest  $\Gamma$  bin,  $b_1$ , to avoid numerical oscillation due to the step function represented by equations (61) and (65). Nevertheless, detailed functional forms of the injected particle spectrum little affect the results.

### 3.5. Gap Position vs. Particle Injection

Let us briefly examine how the gap position changes as a function of  $j^{\text{in}}$  and  $j^{\text{out}}$ . For a detailed argument, see § 2.4 in Paper VII. Defining the particle spatial number density by

$$\bar{n}_{\pm} \equiv \int_1^{\infty} d\Gamma n_{\pm}(\xi, \Gamma), \quad (67)$$

we can rewrite the Poisson equation (11) as

$$\frac{dE_{\parallel}}{d\xi} = \frac{B(\xi)}{B^{\text{in}}} [n_{\text{gap}}(\xi) + f_{\text{null}}(\xi)], \quad (68)$$

where the created charge density in the gap is defined as

$$en_{\text{gap}}(\xi) \equiv e \{ \bar{n}_+(\xi) - j^{\text{in}} - [\bar{n}_-(\xi) - j^{\text{out}}] \} \quad (69)$$

and

$$f_{\text{null}}(\xi) \equiv j^{\text{in}} - j^{\text{out}} + \frac{B^z(\xi)}{B(\xi)}; \quad (70)$$

the two-dimensional screening effect (i.e., the  $-\psi/\Delta_{\perp}^2$  term) is neglected in equation (68). The created charge density increases outward due to discharge and satisfies

$$\begin{aligned} n_{\text{gap}}(\xi^{\text{in}}) &= -j_{\text{gap}}, \\ n_{\text{gap}}(\xi^{\text{out}}) &= j_{\text{gap}}. \end{aligned} \quad (71)$$

We have  $n_{\text{gap}} < 0$  and  $f_{\text{null}} > 0$  in the inner part of the gap, while we have  $n_{\text{gap}} > 0$  and  $f_{\text{null}} < 0$  in the outer part. It follows from equation (68) that the created particles partially screen the original electric field. If  $j_{\text{gap}} = j^{\text{in}} - j^{\text{out}} + B^z(\xi^{\text{in}})/B^{\text{in}}$  holds, we obtain  $dE_{\parallel}/d\xi = 0$  at the inner boundary; that is, the gap is quenched due to the overfilling of space charges.

Then, how about the injected particles? We consider the following three cases:

- $j^{\text{in}} = j^{\text{out}}, j^{\text{gap}} \ll 1$

In this case,  $E_{\parallel}$  maximizes (i.e.,  $f_{\text{null}}$  vanishes) at the

point where  $B^z = 0$  holds. That is, the gap is located around the null surface.

- $j^{\text{in}} \sim 1, j^{\text{out}} \sim 0, j^{\text{gap}} \ll 1$

In this case  $E_{\parallel}$  maximizes at the point where  $B^z = -B$  holds. That is, the gap is located near to the light cylinder.

- $j^{\text{in}} \sim 0, j^{\text{out}} \sim 1, j^{\text{gap}} \ll 1$

In this case  $E_{\parallel}$  maximizes at the point where  $B^z = B$  holds. That is, the gap is located near to the polar cap surface.

In short, created particles in the gap could quench the gap, while injected particles consisting of a single charge only shift it.

#### 4. Constrained Interpolation Profile Method

As we have described, the set of Maxwell and Boltzmann equations consist of equations (10), (11), (18), (19), and (57). The Poisson equation and the  $\gamma$ -ray Boltzmann equations are ordinary differential equations, which can be straightforwardly solved by a simple discretization. In this section, we concentrate on how to solve the hyperbolic-type partial differential equations (18) and (19). Readers who are not interested in numerical techniques may skip to § 5.

The left-hand sides of equation (18) and (19) represent the advection of functional form of  $n_+$  and  $n_-$ , respectively, along the characteristics in the phase space  $(\xi, \Gamma)$ . On the other hand, the right-hand sides describe the collisions. We split these hyperbolic equations into two phases in one single  $\xi$  step. In the advection phase, the non-conservative form having Lagrange differentiation on the left-hand side, is solved analytically in a common and problem-independent way by cubic (or some other order) polynomials. In the non-advection phase, the right-hand side depends on specific problems and is solved by the finite-difference method.

To solve the advection phase (i.e., equations [18] and [19] with  $S = 0$ ), we adopt the semi-Lagrangian scheme, which describes the evolution of the distribution functions based on a reference frame moving with an individual parcel of the distribution function (or the ‘fluid’ in hydrodynamic terminology) like a fully Lagrangian method but make use of an Eulerian computational grid. In this scheme, We choose the set of the parcels at every  $\xi$  step (or ‘time’ step in HD terminology) so that all the parcels arrive at each grid point of the regularly spaced Eulerian mesh in the  $\Gamma$

direction (or a ‘spatial direction’ in HD terminology) at the next  $\xi$  step.

To describe the method as general as possible, we consider the following form of one-dimensional, first-order hyperbolic type differential equation,

$$\frac{\partial f}{\partial \xi} + u(\xi, \Gamma) \frac{\partial f}{\partial \Gamma} = S(\xi, \Gamma). \quad (72)$$

When the velocity  $u$  is constant and  $S = 0$ , it gives a simple translational motion of a wave with velocity  $u$ . In the first-order upwind scheme, numerical diffusion arises when we construct the profile by a linear interpolation. In the Lax-Wendroff scheme, on the other hand, the model suffers overshooting when we use a quadratic polynomial for interpolation.

This decline in accuracy comes from the fact that we neglected the behavior of the solution inside the grid cell and merely follow the smoothness of the solution. It is, therefore, important to develop a method incorporating the real solution into the profile with a grid cell. In this context, Yabe and Aoki (1991) and Yabe et al. (1991) proposed a method to interpolate the intra-grid profiles with cubic polynomials. In this Cubic Interpolated Propagation scheme, not only  $f(\xi, \Gamma)$  but also  $\partial f / \partial \Gamma$  is transported along the characteristics and are interpolated with cubic polynomials. This scheme is completely different from conventional semi-Lagrangian method. In the latter method, the gradient is calculated based on the functional values at the neighboring grid points either by assuming the continuity of the quantities and their first-order (and sometimes higher-order) derivatives at the mesh boundaries (Purnell 1975), or by using approximations based on local grid points (Williamson & Rasch 1989). By a special treatment of the first-order derivatives of the interpolation function, the CIP method achieves a compact form that uses only one mesh cell to construct the interpolation profile.

The CIP method, a sophisticated method for the advection equation, has been under development since the middle of 1980s (Takewaki & Yabe 1987). This method has been applied to various multi-phase flows like milk-crown formation (Yabe, T. 1997; Yabe et al. 1998; Zhang & Yabe 1999), and laser-induced melting, evaporation (Yabe & Xiao 1995). Subsequently, Tanaka et al. (2000) and Yabe et al. (2001) improved the conservative property of advection equations, by introducing fourth-order polynomials to constrain  $f$ ,  $\partial f / \partial \Gamma$  and cell-integrated average (i.e., particle number). Since this scheme uses fourth-order

polynomials, rather than cubic ones, they redefine the name of CIP as Constrained Interpolation Profiles and keep the abbreviation CIP.

In our current problem, advection of initially  $\delta$ -function-like distribution functions becomes important in certain situations. In other words, not only the advection of  $f$  and  $\partial f/\partial\Gamma$ , but also that of  $\partial^2 f/\partial\Gamma^2$  could be important. Therefore, in the present paper, we propose a new higher-order scheme using quintic polynomials to interpolate  $f$ ,  $\partial f/\partial\Gamma$ , and  $\partial^2 f/\partial\Gamma^2$ , extending the concept of the original CIP method.

We describe the basic ideas of time-splitting in CIP scheme in § 4.1, then present a new method of quintic interpolation for the advection-phase computation in § 4.2, and briefly present how to compute particle density in § 4.3. We summarize the numerical method how to apply the CIP scheme to the present problem in § 4.4

#### 4.1. Time Splitting

In the same manner as in the original cubic interpolation, we differentiate equation (72) with respect to  $\Gamma$  to obtain

$$\frac{\partial g}{\partial \xi} + u \frac{\partial g}{\partial \Gamma} = - \frac{\partial u}{\partial \Gamma} g + \frac{\partial S}{\partial \Gamma}, \quad (73)$$

where

$$g(\xi, \Gamma) \equiv \frac{\partial f}{\partial \Gamma}. \quad (74)$$

Since  $g$  is also predicted after propagation, the function after one  $\xi$  step can be limited to a specific profile. If both the values of  $f$  and  $g$  are given at two grid points, the profile between these two points can be interpolated by a cubic polynomial  $F(\Gamma) = C_3\Gamma^3 + C_2\Gamma^2 + C_1\Gamma + C_0$ . This is the original CIP method.

We extend this idea into quintic interpolation. Differentiating equation (73) with respect to  $\Gamma$  once again, we obtain

$$\frac{\partial h}{\partial \xi} + u \frac{\partial h}{\partial \Gamma} = - \frac{\partial u}{\partial \Gamma} h + \frac{\partial}{\partial \Gamma} \left( - \frac{\partial u}{\partial \Gamma} g + \frac{\partial S}{\partial \Gamma} \right) \quad (75)$$

where

$$h(\xi, \Gamma) \equiv \frac{\partial^2 f}{\partial \Gamma^2}. \quad (76)$$

We split the computation into two phases in a single  $\xi$  step. In the advection phase, we solve the homogeneous part of equations (72), (73), and (75),

$$\frac{\partial f}{\partial \xi} + u \frac{\partial f}{\partial \Gamma} = 0, \quad (77)$$

$$\frac{\partial g}{\partial \xi} + u \frac{\partial g}{\partial \Gamma} = 0, \quad (78)$$

$$\frac{\partial h}{\partial \xi} + u \frac{\partial h}{\partial \Gamma} = 0. \quad (79)$$

We denote the corresponding solutions as  $\tilde{f}$ ,  $\tilde{g}$ , and  $\tilde{h}$ , respectively.

After the advection phase is solved, the results of  $\tilde{f}$ ,  $\tilde{g}$ , and  $\tilde{h}$  are advanced to the values of the next  $\xi$  step  $f^k$ ,  $g^k$ , and  $h^k$ . The non-advection phase can be solved by using the conventional finite-difference method.

First, equation (72) gives the value of  $f(\xi^k, b_l)$  as

$$f_l^k = \tilde{f}_l^k + S_l^k D^k, \quad (80)$$

where  $\tilde{f}$  is used to evaluate  $S_l^k$  by equation (44). Secondly, equation (73) gives

$$g_l^k = \tilde{g}_l^k + \left[ - \left( \frac{\partial u}{\partial \Gamma} \right)_l^k \tilde{g}_l^k + \left( \frac{\partial S}{\partial \Gamma} \right)_l^k \right] D^k \quad (81)$$

Generally speaking, it is not easy to obtain a finite-difference form of  $\partial S/\partial\Gamma$ . In this paper, we estimate them with centered finite difference as follows:

$$\begin{aligned} g_l^k &= \tilde{g}_l^k - \left( \frac{\partial u}{\partial \Gamma} \right)_l^k \tilde{g}_l^k D^k \\ &+ \frac{f_{l+1}^k - \tilde{f}_{l+1}^k - (f_{l-1}^k - \tilde{f}_{l-1}^k)}{\Delta_{l+1} + \Delta_l}, \end{aligned} \quad (82)$$

where the grid interval is defined as

$$\Delta_l \equiv b_l - b_{l-1}. \quad (83)$$

That is, the  $\xi$  evolution of  $\partial S/\partial\Gamma$  is estimated by the  $\xi$  evolution of  $\tilde{f}$  already computed by equation (77). Thirdly, equation (75) gives

$$\begin{aligned} h_l^k &= \tilde{h}_l^k - \left( \frac{\partial u}{\partial \Gamma} \right)_l^k \tilde{h}_l^k D^k \\ &+ \frac{g_{l+1}^k - \tilde{g}_{l+1}^k - (g_{l-1}^k - \tilde{g}_{l-1}^k)}{\Delta_{l+1} + \Delta_l}, \end{aligned} \quad (84)$$

Computation of non-advection phase (eq. [80], [82], and [84]) is straightforward. In the next subsection, we describe how to solve equations (77), (78), (79) in the advection phase.

#### 4.2. Advection-phase Computation

By making use of a Lagrange invariant of equation (72), we can compute the time development of  $f$  as

$$f(\xi^k, b_l) = f(\xi^{k-1}, b_l - u_l^k D^k) \quad (85)$$

In the right-hand side,  $f$  is given only at the grid points  $\Gamma = b_1, b_2, \dots, b_{l_m}$ . Noting that the CIP method is a kind of upwind methods, we can construct a piecewise interpolation function  $F(\Gamma)$  in each interval  $[b_{l-1}, b_l]$  to represent  $f(\xi^{k-1}, b_l - u D^k)$  if  $u > 0$ . (If  $u < 0$ , the interval becomes  $[b_{l+1}, b_l]$ .) It should be noted that the Courant-Freidrichs-Lowy (CFL) number is assumed to be less than unity here. In another word, the information is assumed to be transported from a neighboring grid interval. Thus, the  $l$ th function piece  $F_l(\Gamma)$  is determined so as to satisfy

$$\begin{aligned} F(b_{l-1}) &= f(\xi^{k-1}, b_{l-1}), & F(b_l) &= f(\xi^{k-1}, b_l), \\ \frac{\partial F(b_{l-1})}{\partial \Gamma} &= g(\xi^{k-1}, b_{l-1}), & \frac{\partial F(b_l)}{\partial \Gamma} &= g(\xi^{k-1}, b_l), \\ \frac{\partial^2 F(b_{l-1})}{\partial \Gamma^2} &= h(\xi^{k-1}, b_{l-1}), & \frac{\partial^2 F(b_l)}{\partial \Gamma^2} &= h(\xi^{k-1}, b_l). \end{aligned} \quad (86)$$

In order to satisfy these conditions, we consider the following fifth-order polynomial:

$$\begin{aligned} F(\Gamma) &= C_5 \left( \frac{\Gamma - b_l}{\Delta_l} \right)^5 + C_4 \left( \frac{\Gamma - b_l}{\Delta_l} \right)^4 \\ &+ C_3 \left( \frac{\Gamma - b_l}{\Delta_l} \right)^3 + \frac{h_l^{k-1}}{2} (\Gamma - b_l)^2 \\ &+ g_l^{k-1} (\Gamma - b_l) + f_l^{k-1} \end{aligned} \quad (87)$$

Imposing the three conditions in equation (86) at  $\Gamma = b_{l-1}$  (or  $b_{l+1}$  if  $u > 0$ ), we obtain

$$\begin{aligned} C_5 &= 12(f_{lup}^{k-1} - f_l^{k-1}) - 6(g_{lup}^{k-1} + g_l^{k-1})\Delta_l \\ &+ (h_{lup}^{k-1} - h_l^{k-1})\Delta_l^2, \end{aligned} \quad (88)$$

$$\begin{aligned} C_4 &= -30(f_{lup}^{k-1} - f_l^{k-1}) + (14g_{lup}^{k-1} + 16g_l^{k-1})\Delta_l \\ &+ (-2h_{lup}^{k-1} + 3h_l^{k-1})\Delta_l^2, \end{aligned} \quad (89)$$

$$\begin{aligned} C_3 &= 20(f_{lup}^{k-1} - f_l^{k-1}) - 4(2g_{lup}^{k-1} + 3g_l^{k-1})\Delta_l \\ &+ (h_{lup}^{k-1} - 3h_l^{k-1})\Delta_l^2, \end{aligned} \quad (90)$$

where

$$lup \equiv \begin{cases} l-1 & \text{if } u_l^k > 0, \\ l+1 & \text{if } u_l^k < 0, \end{cases} \quad (91)$$

$$\Delta_l \equiv b_{lup} - b_l \quad (92)$$

By substituting equations (88)-(90) into equation (87), we can compute the value of  $f$  at  $\xi = \xi^k$  as

$$f(\xi^k, b_l) = f(\xi^{k-1}, b_l - u_l^k D^k) = F(b_l - u_l^k D^k). \quad (93)$$

We should not stop here. The CIP method belongs to a class of semi-Lagrangian scheme (Staniforth & Cote 1991), which employs separate treatment of the advection term from other terms, and hence enables the advection calculation with large  $\xi$  steps free from the CFL condition. That is, we can choose the step as  $D^k = \xi^k - \xi^{k-1} > \Delta_l/u$ . In this case, the upstream departure point of the characteristic passing through  $(\xi^k, b_l)$  is no longer located in the neighboring grid interval. Instead, we have to calculate the upstream point as

$$\Gamma_{p(l)} = b_l + \int_{\xi^k}^{\xi^{k-1}} u(\xi, \Gamma) d\xi, \quad (94)$$

and define the grid interval in which the upstream point resides as

$$\begin{cases} \Gamma_{n(l)-1} < \Gamma_{p(l)} < \Gamma_{n(l)} & \text{for } u > 0 \\ \Gamma_{n(l)} < \Gamma_{p(l)} < \Gamma_{n(l)+1} & \text{for } u \leq 0 \end{cases} \quad (95)$$

Instead of  $\Delta_l$ , we introduce

$$\Delta_{n(l)} \equiv \Gamma_{p(l)} - \Gamma_{n(l)} \quad (96)$$

to obtain

$$\begin{aligned} f_l^k &= C_5 \Delta_{n(l)}^5 + C_4 \Delta_{n(l)}^4 + C_3 \Delta_{n(l)}^3 \\ &+ \frac{h_{n(l)}^{k-1}}{2} \Delta_{n(l)}^2 + g_{n(l)}^{k-1} \Delta_{n(l)} + f_{n(l)}^{k-1}, \end{aligned} \quad (97)$$

$$\begin{aligned} g_l^k &= 5C_5 \Delta_{n(l)}^4 + 4C_4 \Delta_{n(l)}^3 + 3C_3 \Delta_{n(l)}^2 \\ &+ h_{n(l)}^{k-1} \Delta_{n(l)} + g_{n(l)}^{k-1}, \end{aligned} \quad (98)$$

$$h_l^k = 20C_5 \Delta_{n(l)}^3 + 12C_4 \Delta_{n(l)}^2 + 6C_3 \Delta_{n(l)} + h_{n(l)}^{k-1}. \quad (99)$$

The set of these three equations (97)-(99) gives the evolution of  $f$ ,  $\partial f / \partial \Gamma$ , and  $\partial^2 f / \partial \Gamma^2$ , where  $\Delta_l$  appearing in the definitions of  $C_5$ ,  $C_4$ , and  $C_3$  in equations (88)-(90) should be replaced with  $\Delta_{n(l)}$ .

#### 4.3. Particle Number Density

Before turning to a closer examination of the set of Maxwell and Boltzmann equations, a few remarks

should be made concerning the particle number density. In the case when  $\text{CFL} < 1$ , the density in the Lorentz factor interval  $[b_{l-1}, b_l]$  is obtained by

$$\begin{aligned} \rho_l &= \int_{b_l - u_l^{k-1} D^k}^{b_l} F(\Gamma) d\Gamma \\ &= - \left[ \frac{C_5}{6} \delta_\gamma^5 + \frac{C_4}{5} \delta_\gamma^4 + \frac{C_3}{4} \delta_\gamma^3 + \frac{h_l^{k-1}}{6} \delta_\gamma^2 \right. \\ &\quad \left. + \frac{g_l^{k-1}}{2} \delta_\gamma + f_l^{k-1} \right] \delta_\gamma, \end{aligned} \quad (100)$$

where  $\delta_\gamma \equiv -u_l^{k-1} D^k$ , and  $F(\Gamma)$  is defined by equations (87)-(90). An extension of this method to  $\text{CFL} > 1$  is straightforward. That is, we have to use the upstream departure points passing through  $(\xi^k, b_{l-1})$  and  $(\xi^k, b_l)$  as the lower and upper bound in the integral (see eq. [94]), instead of  $[b_l - u_l^{k-1} D^k, b_l]$ . The particle number contained in a certain Lorentz factor interval (say,  $[b_{l-1}, b_l]$ ) increases at the ‘shock’, because the integration interval (i.e., the Lorentz factor interval between the two upstream departure points) enlarges if characteristics converge.

#### 4.4. Summary of the method

Let me summarize the main points that have been made in §§ 3 and 4.

- (A) We solve the set of Maxwell and Boltzmann equations (10), (11), (18), (19), and (55), under boundary conditions given in § 3.4.
- (B) Ordinary differential equations (10), (11), and (55) can be integrated with a simple discretization.
- (C) Partial differential equations (18) and (19) are solved by the CIP method.
- (D) The free boundaries ( $\xi^{\text{in}}$  and  $\xi^{\text{out}}$ ) are determined such that the electric field vanishes at the outer boundary and that the created pairs give the pre-determined current density  $j_{\text{gap}}$ , which should be specified externally. (For the reasons why the created current in the gap can be treated as a free parameter, see § 4.1 in Paper IX).

### 5. Application to Individual Pulsars

To solve the set of differential equations, we must specify the X-ray field,  $dF_s/d\epsilon_s$ , which is necessary to compute the pair-production redistribution function (eq. [39]). In this paper, we use the X-ray fluxes and

spectra observed for individual rotation-powered pulsars to specify  $dF_s/d\epsilon_s$ . In § 5.1, we summarize the observed properties of the X-ray field. Then we apply the theory to the Vela pulsar in § 5.2, to B1706-44 in § 5.3, to the Geminga pulsar in § 5.4, and to B1055-52 in § 5.5. We assume that the solid angle of the emitted  $\gamma$ -rays is 1 ster throughout this paper.

#### 5.1. Input Soft Photon field

We consider the photons emitted from the neutron star surface as the seed photons for  $(\gamma\gamma)$  pair-production and IC scatterings. That is, we do not consider power-law X-ray components, because they are probably magnetospheric and beamed away from the accelerator. We evaluate the IR photon field, which is needed to compute the IC scattering rate, from the Rayleigh-Jeans tail of the surface (blackbody) component. In table 1, we present the observed properties of the four  $\gamma$ -ray pulsars exhibiting surface X-ray components, in order of spin-down luminosity,  $L_{\text{spin}}$ .

**Vela** (J0835-4513) From Chandra observations in 0.25-8.0 keV, the spectrum of this pulsar is turned out to consist of two distinct component: A soft component and a hard, power-law component. The hard component is probably a magnetospheric origin and hence will be beamed away from the gap. Thus, we consider only the soft component as the X-ray field illuminating the outer gap. This component can be modeled either as a blackbody spectrum with  $kT = 1.49\text{MK}$  and  $A_s = 0.044A_*(d/0.25)^2$ , or as a magnetic hydrogen atmosphere spectrum with effective temperature  $kT = 0.68\text{MK}$  (Pavlov et al. 2001). Based on high-resolution Ca II and Na I absorption-line spectra toward 68 OB stars in the direction of the Vela supernova remnant, Cha, Sembach, and Danks (1999) determined the distance to be  $250 \pm 30$  pc. **B1706-44** (J1710-4432) Gotthelf, Halpern, Dodson (2002) reported a broad, single-peaked pulsed profile with pulsed fraction of 23%, using the High Resolution Camera on-board the Chandra X-ray observatory. They fitted the spectroscopic data to find (at least) two components, e.g., a blackbody of  $kT = 143$  eV with  $A = 0.129A_*$  and a power-law component with photon index of  $-2.0$ . We consider that the former component illuminates the gap efficiently and neglect the second one. We adopt  $d = 2.5$  kpc as a compromise between the smaller dispersion-measure distance of 1.8 kpc based on the free electron model by Taylor and Cordes (1993) and the larger H I kine-

Table 1: Input thermal X-ray field

pulsar	$\lg L_{\text{spin}}$ ergs $\text{s}^{-1}$	distance kpc	$\Omega$ $\text{rad s}^{-1}$	$\lg B_s$ G	$kT_s$ eV	$A_s/A_*$	$kT_h$ eV	$A_h/A_*$	model	refs.
Vela	36.84	0.25	70.4	12.53	128 59	0.048 1.000	...	...	blackbody hydrogen atm.	1, 2 1
B1706-44	36.53	2.50	61.3	12.49	143	0.129	...	...	blackbody	3
Geminga	34.51	0.16	26.5	12.21	48	0.160	...	...	blackbody	4, 5
B1055-52	34.48	1.53	31.9	12.03	68	7.300	320	$10^{-3.64}$	blackbody	6

1: Pavlov et al. 2001; 2: Ögelman et al. 1993; 3: Gotthelf, Halpern, Dodson 2002; 4: Halpern & Wang 1997; 5: Becker & Trümper 1996; 6: Greiveldinger et al. 1996;

matic distance of 2.4–3.2 kpc derived by Koribalski et al. (1995).

**Geminga** (J0633+1746) The X-ray spectrum consists of two components: the soft surface blackbody with  $kT_s = 50$  eV and  $A_s = 0.22A_*(d/0.16)^2$  and a hard power law with  $\alpha = -1.6$  (Halpern & Wang 1997). A parallax distance of 160pc was estimated from HST observations (Caraveo et al. 1996).

**B1055–52** (J1059–5237) Combining ROSAT and ASCA data, Greiveldinger et al. (1996) reported that the X-ray spectrum consists of two components: a soft blackbody with  $kT_s = 68$  eV and  $A_s = 7.3A_*(d/1.53)^2$  and a hard blackbody with  $kT_h = 320$  eV and  $A_h = 2.3 \times 10^{-4}(d/1.53)^2$ . The distance is estimated to be 1.53 kpc from dispersion measure (Taylor & Cordes 1993).

## 5.2. The Vela pulsar

We first apply the theory to the Vela pulsar, using the X-ray field modeled by the blackbody spectrum in § 5.2.1–5.2.3, and by the hydrogen atmosphere spectrum in § 5.2.4.

### 5.2.1. Acceleration Field and Characteristics

Let us first consider the spatial distribution of the acceleration field,

$$-\frac{d\Psi}{ds} = \frac{\omega_p}{c} \frac{m_e c^2}{e} E_{\parallel}(\xi) \quad [\text{V m}^{-1}], \quad (101)$$

which is solved from the Poisson equation (11). As demonstrated in § 3.5, an external particle injection only shifts the gap, while the created current density satisfying  $j_{\text{gap}} = j^{\text{in}} - j^{\text{out}} + B^z(\xi^{\text{in}})/B^{\text{in}}$  quenches it. Since this  $j_{\text{gap}}$  is typically a few percent for young pulsars like Vela, we consider a small created current density,  $j_{\text{gap}} = 1.0 \times 10^{-4}$ .

To compare the effects of particle injection, we present the  $E_{\parallel}$  distribution for the three cases of  $j^{\text{in}} = 0$  (solid), 0.25 (dashed), and 0.50 (dash-dotted) in figure 2. The magnetic inclination is chosen to be  $\alpha_i = 75^\circ$ . We adopt  $j^{\text{out}} = 0$  throughout this paper, unless its value is explicitly specified. The abscissa denotes the distance along the last-open field line normalized by  $\varpi_{\text{LC}}$ .

As the solid line shows,  $E_{\parallel}$  is located around the null surface when there is no particle injection across either of the boundaries. Moreover,  $E_{\parallel}$  varies quadratically, because the Goldreich-Julian charge density deviates from zero nearly linearly near to the null surface.

As the dashed and dash-dotted lines indicate, the gap shifts outwards as  $j^{\text{in}}$  increases. When  $j^{\text{in}} = 0.5$  for instance, the gap is located on the half way between the null surface and the light cylinder. This result is consistent with Papers VII, VIII, and IX, in which the mono-energetic approximation was adopted for the particle energy distribution.

In figure 3, we present the characteristics of partial differential equation (18) for positrons by solid lines, together with  $E_{\parallel}(\xi)$  when  $j^{\text{in}} = 0.25$  and  $\alpha_i = 75^\circ$  (i.e., the dashed line in fig. 2). We also superpose the equilibrium Lorentz factor that would be obtained if we assumed the balance between the curvature radiation reaction and the electrostatic acceleration, as the dotted line. It follows that the particles are not saturated at the equilibrium Lorentz factor in most portions of the gap.

In the outer part of the gap where  $E_{\parallel}$  is decreasing, characteristics begin to concentrate; as a result, the energy distribution of outwardly propagating particles forms a ‘shock’ in the Lorentz factor direction. However, the particle Lorentz factors do not match

the equilibrium value (dotted line). For example, near the outer boundary, the particles have larger Lorentz factors compared with the equilibrium value, because the curvature cooling scale is longer than the gap width. Thus, we must discard the mono-energetic approximation that all the particles migrate at the equilibrium Lorentz factor as adopted in Papers I through IX. We instead have to solve the energy dependence of the particle distribution functions explicitly.

The particles emit  $\gamma$ -rays not only inside of the gap but also outside of it, being decelerated by the curvature radiation-reaction force. The length scale of the deceleration is given by

$$\begin{aligned} l_{\text{dec}} &= c \cdot \frac{\Gamma m_e c^2}{\frac{2e^2}{3c^3} \Gamma^4 \left(\frac{c^2}{\rho_c}\right)^2} \\ &= 0.4 \varpi_{\text{LC}} \Omega_2^{-1} \left(\frac{\Gamma}{10^7}\right)^{-3} \left(\frac{\rho_c}{\varpi_{\text{LC}}/2}\right)^2 \quad (102) \end{aligned}$$

Since the typical Lorentz factor is a few times of  $10^7$ ,  $l_{\text{dec}}$  is typically much less than  $\varpi_{\text{LC}}$ . Therefore, the escaping particles lose their energy well inside of the light cylinder.

### 5.2.2. Particle Energy Distribution

As we have seen in the foregoing subsection, the distribution function of the outwardly propagating particles forms a ‘shock’ in the outer part of the gap. In figure 4, we present the energy distribution of particles at several representative points along the field line. At the inner boundary ( $s = 0.184\varpi_{\text{LC}}$ ), particles are injected with Lorentz factors typically less than  $2 \times 10^6$  as indicated by the solid line. Particles migrate along the characteristics in the phase space and gradually form a ‘shock’ as the dashed line (at  $s = 0.204\varpi_{\text{LC}}$ ) indicates, and attains maximum Lorentz factor at  $s = 0.226\varpi_{\text{LC}}$  as the dash-dotted line indicates. Then they begin to be decelerated gradually and escape from the gap with large Lorentz factors  $\sim 2.5 \times 10^7$  (dotted line) at the outer boundary,  $s = s^{\text{out}} = 0.241\varpi_{\text{LC}}$ .

Even though the ‘shock’ is captured by only a few grid points for the dash-dotted line in figure 4, the CIP scheme accurately satisfies the conservation of the total current density,

$$\begin{aligned} j_{\text{tot}} &= n_+(\xi) + n_-(\xi) \\ &= j^{\text{in}} + j^{\text{out}} + j_{\text{gap}} \approx j^{\text{in}}. \quad (103) \end{aligned}$$

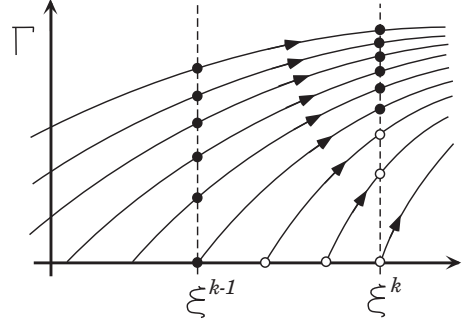


Fig. 1.— Schematic picture of characteristics in the phase space  $(\xi, \Gamma)$ . Positrons (or electrons) move along these characteristics when  $E_{\parallel} > 0$  (or  $E_{\parallel} < 0$ ). The filled circles indicate the particles moved from  $\xi = \xi^{k-1}$  to  $\xi^k$  in a certain time interval. Created particles (open circles) are assumed to migrate immediately outwards after the birth.

J0835–4513

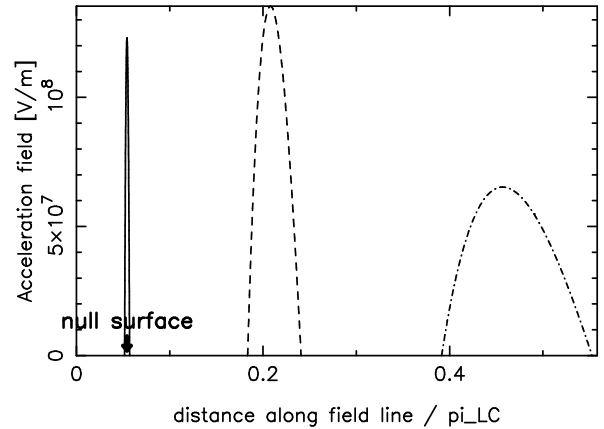


Fig. 2.— Spatial distribution of  $-d\Psi/ds$  for  $j^{\text{in}} = 0$  (solid), 0.25 (dashed), and 0.5 (dash-dotted), for the Vela pulsar when  $\alpha_i = 75^\circ$  and  $j_{\text{gap}} = 1.0 \times 10^{-4}$  and  $j^{\text{out}} = 0$ . The abscissa designates the distance along the last-open field line normalized by the light cylinder radius.

The result of  $j_{\text{tot}} = n_+ + n_-$  for this case (i.e.,  $j^{\text{in}} = 0.25$ ) is shown in figure 5. It follows that the particle number is accurately computed even at the ‘shock’.

### 5.2.3. Formation of Power-law Gamma-ray Spectrum

So far, we have seen that the outwardly propagating particles are not saturated at the equilibrium value and that such particles escape from the gap with sufficient Lorentz factors suffering subsequent cooling via curvature process. It seems, therefore, reasonable to suppose that a significant fraction of the  $\gamma$ -ray luminosity is emitted from such escaping particles.

We present the  $\gamma$ -ray spectrum emitted from outwardly propagating particles (i.e., positrons) for the Vela pulsar with  $\alpha_i = 75^\circ$ ,  $j_{\text{gap}} = 1.0 \times 10^{-4}$ ,  $j^{\text{in}} = 0.25$  in figure 6. The dashed line represents the  $\gamma$ -ray flux emitted within the gap, while the solid one includes that emitted outside of the gap by the escaping particles. Therefore, the difference between the solid and the dashed lines indicates the  $\gamma$ -ray flux emitted by the particles migrating outside of the gap. For comparison, we plot the phase-averaged EGRET spectrum, which is approximated by a power law with a photon index  $-1.7$  (Kanbach et al. 1994).

It follows from the figure that the  $\gamma$ -ray spectrum in 100 MeV–GeV energies can be explained by the curvature radiation emitted by the escaping particles. We adjusted the transfield thickness as  $D_\perp = 0.16\varpi_{\text{LC}} = 2.8W$  so that the observed flux may be explained. The luminosity of the  $\gamma$ -rays emitted outside of the gap contribute 45% of the total luminosity  $5.11 \times 10^{33} \text{ ergs s}^{-1}$  between 100 MeV and 20 GeV. In another word, we do not have to assume a power-law energy distribution for particles (as assumed in some of the previous outer-gap models) to explain the power-law  $\gamma$ -ray spectrum for the Vela pulsar. This conclusion is natural, because a power-law energy distribution of particles will not be achieved by an electrostatic acceleration, and because magnetohydrodynamic shocks (i.e., real shocks) will not be formed in the accelerator.

Because the X-ray field is dense for this young pulsar, the pair-production mean free path, and hence the gap width becomes small (for details, see Hirotani & Okamoto 1998, Hirotani 2000a, Paper IV; Hirotani 2001, Paper V). As a result, the potential drop in the gap  $2.18 \times 10^{13} \text{ V}$  is only 0.78 % of the electro-

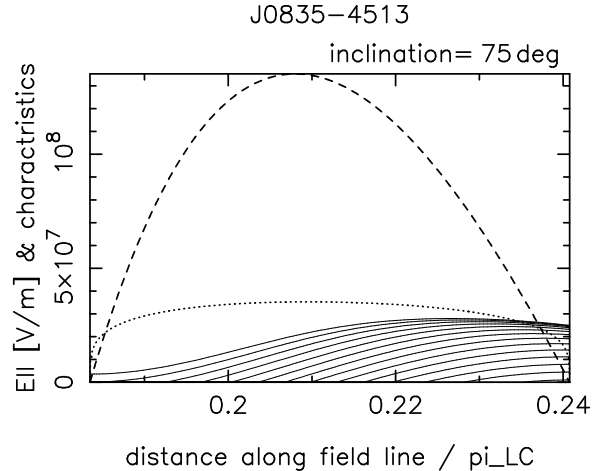


Fig. 3.— Spatial distribution of  $-d\Psi/ds(s)$  (dashed) for the Vela pulsar when  $\alpha_i = 75^\circ$ ,  $j^{\text{in}} = 0.25$ ,  $j^{\text{out}} = 0$ , and  $j_{\text{gap}} = 1.0 \times 10^{-4}$ . The soft photon field is approximated by a single blackbody component. The characteristics are also shown by solid lines. The equilibrium Lorentz factor, which would be obtained if we balanced the curvature radiation-reaction force and the electrostatic force, is indicated by the dotted line.

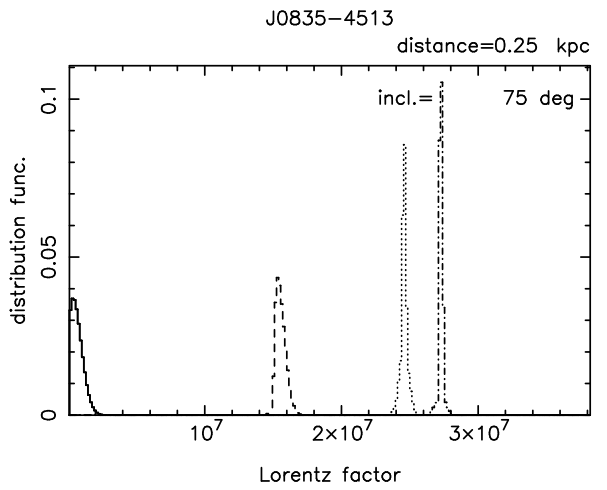


Fig. 4.— Particle energy distribution at several points along the magnetic field lines for the same case as in figure 3. Initial spectrum (solid line) evolves to dashed, dash-dotted, and dotted lines, as particles propagate outwards.

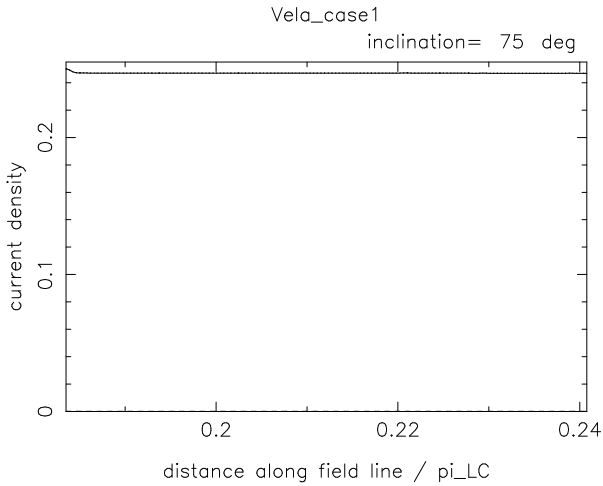


Fig. 5.— Total current is conserved accurately along the field lines for the same case as in figure 3.

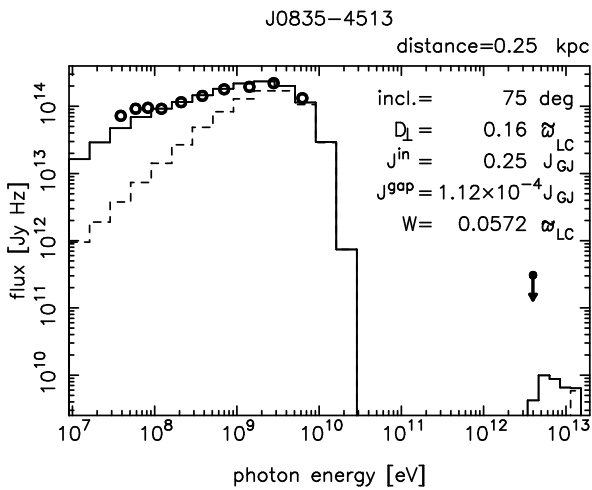


Fig. 6.— Computed  $\gamma$ -ray spectrum for the Vela pulsar for the same case as in figure 3. The dashed line represents the emission from the gap, while the solid one includes the flux emitted by the particles being decelerated via curvature process outside of the gap.

motive force (EMF) exerted on the spinning neutron star surface  $\sim \mu/\varpi_{LC}^2 = 2.79 \times 10^{15}$  V. Nevertheless, this potential drop is enough to accelerate particles into high Lorentz factors,  $10^{7.3}$ .

#### 5.2.4. Hydrogen Atmosphere Model

We next briefly examine the  $\gamma$ -ray spectrum when the soft photon field is modeled as the hydrogen atmosphere spectrum (Pavlov et al. 2001), rather than the blackbody spectrum. In figure 7, we present the resultant spectrum for the same parameter set as in figure 6, except for the fitting model for the observed X-ray field. We fix  $s^{in}$  instead of  $j_{gap}$  for comparison purpose. It follows that the pair production,  $j_{gap}$ , decreases while the IC flux increases for the hydrogen atmosphere model. This is because a blackbody model gives a temperature higher than the effective temperature obtained in hydrogen atmosphere model and an area smaller than the whole neutron star surface. That is, the fewer X-ray photons obtained in hydrogen atmosphere model result in a smaller pair production, while the more IR photons result in a larger IC scatterings. Nevertheless, the obtained solutions little differ between these two fitting models. This is due to the ‘negative feedback effect’ of the gap electrodynamics (Paper V), which ensures the existence of solutions in a wide parameter range and suggests the dynamical stability of the solutions.

#### 5.2.5. Summary for the Vela Pulsar

In both blackbody and the hydrogen atmosphere models, analogous spectra as figures 6 and 7 are obtained for  $45^\circ < \alpha_i < 75^\circ$  and for  $0.125 < j^{in} < 0.250$ . By varying  $\alpha_i$  and  $j^{in}$ , we find that the potential drop in the gap becomes between  $1.4 \times 10^{13}$  V and  $3.6 \times 10^{13}$  V for this range of  $\alpha_i$  and  $j^{in}$ ; it decreases with increasing  $\alpha_i$  and increases with increasing  $j^{in}$ .

For  $45^\circ < \alpha_i < 75^\circ$ ,  $0 < j^{in} < 0.5$ ,  $j^{out} = 0$  (fixed), and appropriately chosen  $j_{gap}$  so that the GeV flux may match the observed one, TeV flux is always less than  $2 \times 10^{10}$  JyHz. Thus, one general point becomes clear: TeV flux is unobservable with current ground-based telescopes, provided that the emission solid angle is as large as 1 ster and that the surface thermal (not magnetospheric) X-rays are upscattered inside and outside of the gap. Since the magnetospheric X-rays will less efficiently illuminate the gap and their specific intensity is highly uncertain, we leave the problem of the upscatterings of magneto-

spheric (power-law) X-rays untouched.

### 5.3. PSR B1706-44

We next apply the theory to a Vela-type pulsar, PSR B1706-44. The computed spectrum is presented in figure 8. The magnetic inclination is assumed to be  $75^\circ$  and we adopt  $j^{\text{in}} = 0.10$ ,  $j^{\text{out}} = 0$ , and  $j_{\text{gap}} = 1.6 \times 10^{-3}$ . The computed spectrum appears to be consistent with observations; however, we must assume a very large perpendicular width  $D_{\perp} = 0.3\varpi_{\text{LC}} = 1.7s^{\text{in}}$ . That is, we cannot obtain the observed flux, unless we adopt an unrealistically large  $D_{\perp}$ . The situation becomes worse if we assume a smaller  $\alpha_i$ . For a greater  $\alpha_i$  (say,  $80^\circ$ ),  $D_{\perp}/s^{\text{in}}$  decreases. However, for such a large  $\alpha_i$ , the ‘outer’ gap is located nearer than  $0.05\varpi_{\text{LC}} \sim 25r_*$  from the star surface. In such a strong  $B$  region, the mono-pitch-angle approximation does not give a correct estimate of the synchro-curvature process; thus, we do not consider such a large  $\alpha_i$  in this paper.

If we were to assume mono-energetic approximation that the outgoing particles are saturated at the equilibrium Lorentz factor (dotted line in fig. 9), the luminosity would increase significantly. This is because the curvature radiation rate [ergs  $\text{s}^{-1}$  (particle) $^{-1}$ ] is proportional to  $\Gamma^4$ . For example, Takata et al. (2002) concluded that the luminosity of PSR B1706-44 can be marginally explained if they adopt  $D_{\perp} = \varpi_{\text{LC}} \sim 2s^{\text{in}}$  under the mono-energetic approximation. However, it follows from figure 9 that particle motion is highly unsaturated throughout the gap. Therefore, we have to discard the mono-energetic approximation and explicitly consider the energy dependence of particles for this young pulsar.

In short, we cannot explain the  $\gamma$ -ray luminosity of B1706-44 with  $d = 2.5$  kpc. The distance should be less than 1.5 kpc so that the gap may have a physically acceptable transfield thickness,  $D_{\perp} < s^{\text{in}}$  for a reasonable  $\alpha_i$  ( $\leq 75^\circ$ ).

### 5.4. The Geminga Pulsar

Let us apply the theory to a cooling neutron star, the Geminga pulsar. Since the soft photon field is less dense compared with young pulsars like Vela and B1706-44, the gap is extended as large as  $W \sim 0.59\varpi_{\text{LC}}$  (for the relationship between the gap width and the soft photon field, see Paper V). We present the spatial distribution of  $E_{\parallel}$  (dashed line) as well as the characteristics (solid lines) and the equilibrium

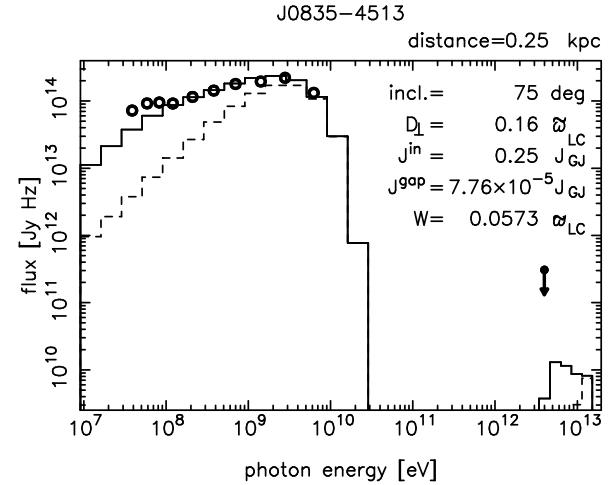


Fig. 7.— Same figure as fig 6, except that the soft photon field is modeled as a hydrogen atmosphere spectrum.

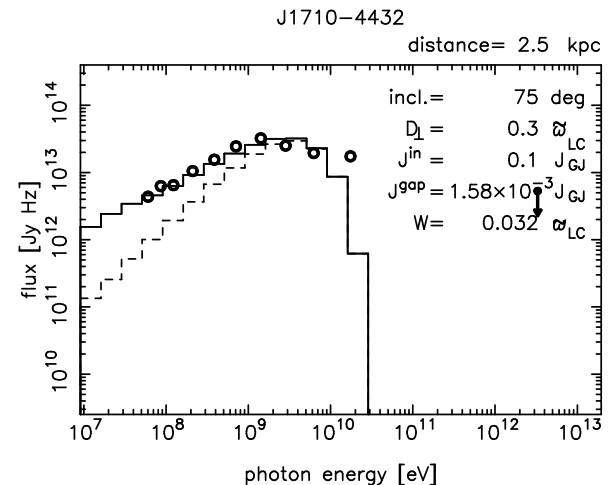


Fig. 8.— Computed  $\gamma$ -ray spectrum for PSR B1706-44. The dashed and solid lines represent the same components as fig 6

Lorentz factor (dotted line) in figure 10. In the outer part of this extended gap,  $\rho_{\text{GJ}}$  gradually increases with the distance,  $s$ . As a result,  $E_{\parallel}(s)$  deviates from quadratic distribution and decrease gradually in the outer part of the gap. Because of this extended feature, particles are nearly saturated at the equilibrium Lorentz factor. In another word, the mono-energetic approximation adopted in Papers I–IX is justified for this middle-aged pulsar. Particle distribution function forms a strong ‘shock’, which is captured only with one grid point, in  $0.4 < s/\varpi_{\text{LC}} < 0.45$ . As a result,  $j_{\text{tot}}$  fluctuates as figure 11 indicates. Nevertheless, it returns to the 0.229 level, which is 8 % less than the value it should be (0.250), as the characteristics begin to be less concentrated beyond  $s = 0.45\varpi_{\text{LC}}$ . In fact, such a ‘recovery’ of  $j_{\text{tot}}$  is commonly seen when the ‘shock’ of a particle energy distribution begins to be captured more than two grid points. This is because the intra-grid profile can be constructed from the higher-order derivatives (i.e.,  $g$  and  $h$  in eqs. [73] and [75]) in CIP scheme. This case (Geminga,  $j^{\text{in}} = 0.25$ ) has the worst accuracy among all the cases considered in this paper. Usually, the current density returns to the original level (0.25 in this case), even if it fluctuates in a limited region in the gap.

In figure 12, we present the resultant  $\gamma$ -ray spectrum. Because of the nearly saturated motion of the particles, they lose most of their energy within the gap. As a result,  $\gamma$ -ray luminosity associated with the escaping particles ( $5.4 \times 10^{31} \text{ ergs s}^{-1}$ ), is negligibly small compare to that emitted within the gap ( $1.02 \times 10^{33} \text{ ergs s}^{-1}$ ), which is represented by the dashed line.

It follows from the figure that the observed, soft spectrum between 200 MeV and 6 GeV can be explained by the present one-dimensional model. It is interesting to compare this result with what obtained for the Vela pulsar (figs. 6 and 7). Between 100 MeV and 1 GeV energies, both spectra are formed by the superposition of the curvature radiation emitted by the particles having different energies at different positions. The important difference is that the particles are saturated at the equilibrium Lorentz factor *in the gap* for the Geminga pulsar, while they are nearly mono-energetic but only decelerated via curvature process *outside of the gap* for the Vela pulsar. Because the particles no longer gain energy from the electric field outside of the gap, particles soon lose energies and emit soft  $\gamma$ -rays compared with those still

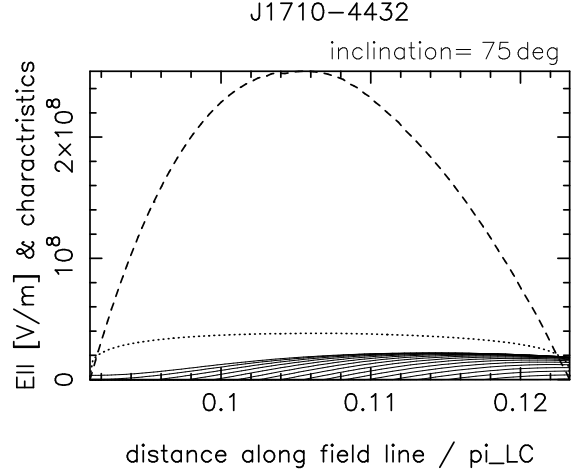


Fig. 9.— Spatial distribution of  $-d\Psi/ds(s)$  (dashed) for PSR B1706-44 when  $\alpha_i = 75^\circ$ ,  $j^{\text{in}} = 0.10$ , and  $j^{\text{out}} = 0$ , and  $j_{\text{gap}} = 1.6 \times 10^{-3}$ . Solid and dotted lines indicate the characteristics and the equilibrium Lorentz factor. Particles are highly unsaturated for this young pulsar.

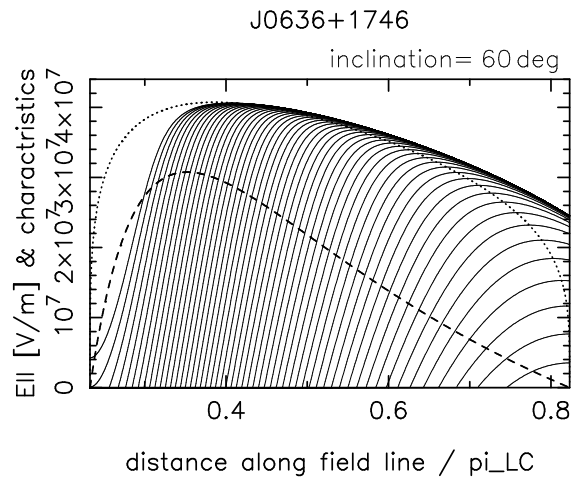


Fig. 10.— Spatial distribution of  $-d\Psi/ds$  (dashed line) for the Geminga pulsar when  $\alpha_i = 60^\circ$ ,  $j^{\text{in}} = 0.25$ ,  $j^{\text{out}} = 0$ , and  $j_{\text{gap}} = 7.8 \times 10^{-5}$ . Particles are saturated at the equilibrium Lorentz factor (dotted line) for this middle-aged pulsar.

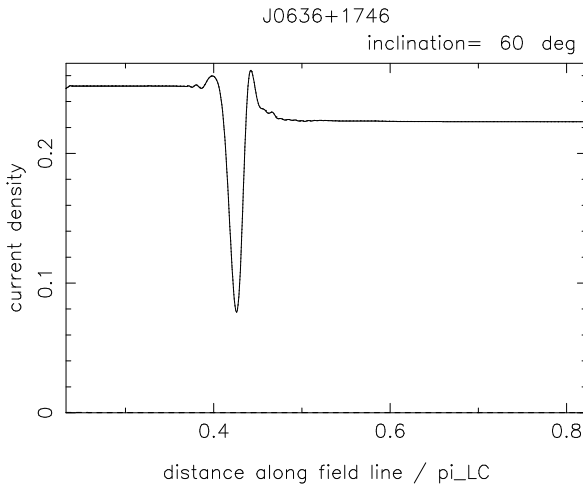


Fig. 11.— Total current density,  $j_{\text{tot}}$ , for the same case as in figure 10. It fluctuates in  $0.4\varpi_{\text{LC}} < s < 0.45\varpi_{\text{LC}}$ , because the particle distribution function forms a strong ‘shock’ in the Lorentz factor direction.

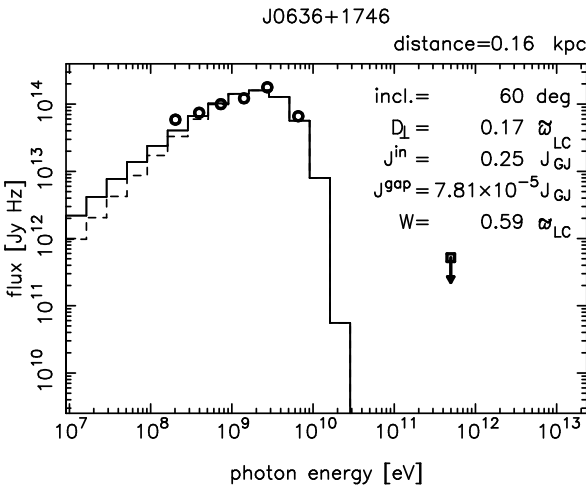


Fig. 12.— Computed  $\gamma$ -ray spectrum for the Geminga pulsar for the same case as in figure 10. The dashed and solid lines represent the same components as figure 6.

being accelerated in the gap. As a result, the  $\gamma$ -ray spectrum for the Vela pulsar becomes softer than that for the Geminga pulsar. Extending this consideration, we can predict that the  $\gamma$ -ray spectrum below GeV energies becomes soft for young pulsars and tends to become hard as the pulsar ages.

### 5.5. PSR B1055-52

Let us finally apply the present theory to another middle-aged pulsar, B1055-52. Since the acceleration field and the particle energy distributions are similar to the Geminga pulsar, we present only the computed  $\gamma$ -ray spectra for this pulsar in figure 13. The solid and dashed lines represent the spectra for the distances 0.50 and 1.53 kpc, respectively. For  $d = 0.50$  kpc,  $j_{\text{gap}} = 4.5 \times 10^{-3}$  is chosen so that the peak energy of curvature radiation may match the observed peak energy. In this case, the gap exists in  $0.1450\varpi_{\text{LC}} < s < 0.3882\varpi_{\text{LC}}$ . For  $d = 1.53$  kpc,  $j_{\text{gap}} = 4.0 \times 10^{-2}$  is chosen and the gap exists in  $0.1475\varpi_{\text{LC}} < s < 0.3818\varpi_{\text{LC}}$ .

It follows from the figure that the solid line matches the observed flux with a reasonable transfield thickness,  $D_{\perp} = 0.61s^{\text{in}} = 0.38W$ . On the other hand, for the dashed line, we have to choose  $D_{\perp} = 0.25\varpi_{\text{LC}} = 1.7s^{\text{in}}$ , which is unrealistic. The observed fluxes cannot be explained with acceptable gap width (e.g.,  $D_{\perp} < s^{\text{in}}$ ) no matter what we may adjust  $j^{\text{in}}$ ,  $j^{\text{out}}$ , and  $j_{\text{gap}}$  if  $d = 1.53$  kpc.

On these grounds, we conjecture that the distance  $1.5 \pm 0.4$  kpc determined from the dispersion measure (Taylor & Cordes 1993) is too large and that a more closer distance, such as 500 pc derived from ROSAT data analysis (Ögelman & Finley 1993) or 700 pc estimated from a study of the extended nonthermal radio source around the pulsar (Combi, Romero, Azcárate 1997), is plausible. This conclusion is consistent with the results obtained in Paper IX under the monoenergetic approximation that all the particles are saturated at the equilibrium Lorentz factor, which is justified for middle-aged pulsars.

## 6. Discussion

In summary, we have quantitatively examined the stationary pair-production cascade in an outer magnetosphere, by solving the set of Maxwell and Boltzmann equations one-dimensionally along the magnetic field lines. We revealed that an accelerator (or a potential gap) is quenched by the created pairs in

the gap but is *not* quenched by the injected particles from outside of the gap, and that the gap position shifts as a function of the injected particle fluxes: If the injection rate across the inner (or outer) boundary approaches the Goldreich-Julian value, the gap is located near to the light cylinder (or the star surface). It should be emphasized that the particle energy distribution is not represented by a power law, as assumed in some of previous outer-gap models. The particles escape from the gap with sufficient Lorentz factors and emit significant photons in 100 MeV–3 GeV energies via curvature radiation especially for young pulsars. The  $\gamma$ -ray spectrum including this component explains the EGRET spectra for Vela, Geminga and PSR B1055-52 between 100 MeV and 6 GeV. TeV fluxes are unobservable with current ground-based telescopes for these pulsars.

We point out an implication to the  $\gamma$ -ray luminosity versus the spin-down luminosity in the next subsection, then discuss future extensions of the present method in §§ 6.2–6.4.

### 6.1. Gamma-ray vs. Spin-down Luminosities

It should be noted that the emission from the escaping particles attain typically 40% of the total  $\gamma$ -ray luminosity for young pulsars. Thus, it is worth mentioning its relationship with the spin-down luminosity,

$$L_{\text{spin}} = -I\Omega\dot{\Omega} \propto \Omega^{n+1}, \quad (104)$$

where the braking index  $n$  is related to the spin-down rate as

$$\dot{\Omega} = -k\Omega^n. \quad (105)$$

If the spin down is due to the magnetic dipole radiation, we obtain  $n = 3$ .

The outwardly propagating particles escape from the gap with spatial number density (eq. [14])

$$N_{\text{out}} = (j^{\text{in}} + j_{\text{gap}}) \frac{\Omega B^{\text{out}}}{2\pi ce}, \quad (106)$$

where  $B^{\text{out}} = B(\xi^{\text{out}})$ . Therefore, the energy carried by the escaping particles per unit time is given by

$$L_{\text{esc}} = D_{\perp}^2 c N_{\text{out}} \Gamma_{\text{esc}} m_e c^2, \quad (107)$$

where  $\Gamma_{\text{esc}} (\sim 10^{7.3})$  refers to the Lorentz factor of escaping particles. Note that  $\Gamma_{\text{esc}}$  is essentially determined by the equilibrium Lorentz factor (dotted

line in fig. 3) near the gap center. Since the equilibrium Lorentz factor depends on the one-fourth power of  $E_{\parallel}$ , the variation of  $\Gamma_{\text{esc}}$  on pulsar parameters is small. We can approximate  $B^{\text{out}}$  as

$$B^{\text{out}} \sim \frac{\mu}{\varpi_{\text{LC}}^3} \left( \frac{\varpi_{\text{LC}}}{r^{\text{out}}} \right)^3, \quad (108)$$

where  $r^{\text{out}}$  refers to the distance of the outer boundary of the gap from the star center. Let us assume that the position of the gap with respect to the light cylinder radius,  $r^{\text{out}}/\varpi_{\text{LC}}$ , does not change as the pulsar evolves; this situation can be realized if  $j^{\text{in}} - j^{\text{out}}$  is unchanged. Evaluating  $B$  at  $r = 0.5\varpi_{\text{LC}}$ , we obtain

$$\begin{aligned} L_{\text{esc}} &= \frac{4\Gamma_{\text{esc}} m_e c}{\pi e} \mu \Omega^2 \left( \frac{D_{\perp}}{\varpi_{\text{LC}}} \right)^2 \\ &\propto L_{\text{spin}}^{0.5}, \end{aligned} \quad (109)$$

where  $n = 3$  is assumed in the second line. To derive this conclusion, it is essential that the particles are not saturated at the equilibrium Lorentz factor. Thus, the same discussion can be applied irrespective of the gap position or the detailed physical processes involved. For example, an analogous conclusion was derived for a polar-cap model by Harding, Muslimov, and Zhang (2002). It is, therefore, concluded that the observed relationship  $L_{\gamma} \propto L_{\text{spin}}^{0.5}$  merely reflects the fact that the particles are unsaturated in the gap and does not discriminate the gap position.

Let us compare this result with what would be expected in the CHR picture. Since the gap is extended significantly along the field lines in the CHR picture, particles are saturated at the equilibrium Lorentz factor to lose most of their energies within the gap, rather than after escaping from it. We can therefore estimate the  $\gamma$ -ray luminosity as

$$L_{\text{gap}} = (D_{\perp} D_{\phi} W) \cdot N_{\text{out}} \cdot P_{\text{SC}} \quad (110)$$

where  $D_{\phi}$  refers to the azimuthal thickness of the gap,  $P_{\text{SC}}$  [ergs  $\text{s}^{-1}$  (particle) $^{-1}$ ] represents the curvature radiation rate. Noting that the particle motion saturates at the equilibrium Lorentz factor satisfying  $P_{\text{SC}}/c = e(-d\Psi/ds)$ , recalling that the acceleration field is given by  $-d\Psi/ds \approx \Omega B D_{\perp}^2 / 4\rho_c c$  in the CHR picture, and evaluating  $B$  at  $r = \varpi_{\text{LC}}$ , we obtain

$$\begin{aligned} L_{\text{gap}} &= \frac{\mu^2 \Omega^4}{4\pi c^3} \frac{D_{\perp}^3 D_{\phi} W}{\varpi_{\text{LC}}^5} \left( \frac{\rho_c}{0.5\varpi_{\text{LC}}} \right)^{-1} \\ &\propto L_{\text{spin}}, \end{aligned} \quad (111)$$

where  $n = 3$  is assumed again in the second line. Even though the escaping particles little contribute to the  $\gamma$ -ray luminosity in the CHR picture, it is worth mentioning the work done by Crusius-Wätzel and Lesch (2002), who accurately pointed out the importance of the escaping particles in the CHR picture, when we interpret  $L_\gamma \propto L_{\text{spin}}^{0.5}$  relation.

As we have seen, the particles being no longer accelerated contribute for the  $\gamma$ -ray luminosity that is proportional to  $L_{\text{spin}}^{0.5}$ . Reminding that the particles migrate with larger Lorentz factors than the equilibrium value in the outer part of the gap (see fig. 3), we can expect roughly half of the  $\gamma$ -ray luminosity is proportional to  $L_{\text{spin}}^{0.5}$  (mainly between 100 MeV and 1 GeV), and the rest of the half to  $L_{\text{spin}}$  (mainly above 1 GeV). As a pulsar ages, its declined surface emission results in a large pair-production mean free path, and hence  $W$ . Because  $|\rho_{\text{GJ}}| \propto r^{-3}$  becomes small in the outer part of such an extended gap,  $E_{\parallel}(\xi)$  deviates from quadratic distribution to decline gradually in the outer part (fig. 10). As a result, particles tend to be saturated at the equilibrium value. On these grounds, we can predict that the  $\gamma$ -ray luminosity tends to be proportional to  $L_{\text{spin}}$  with age, deviating from  $L_{\text{spin}}^{0.5}$  dependence for young pulsars.

In the present paper, we have examined the set of Maxwell and Boltzmann equations one-dimensionally both in the configuration and the momentum spaces (i.e., only  $\xi$  and  $\Gamma$  dependences are considered.) In the next three sections, we discuss the extension of the present method into higher dimensions

## 6.2. Returning Particles

If we discard the mono-pitch-angle approximation represented by equation (16), and consider explicitly the pitch-angle dependence of particle distribution functions, we can compute the synchro-curvature radiation more accurately. Moreover, we can also consider the returning motion of particles in the gap. The returning motion becomes particularly important when both signs of charge are injected across the boundary. For example, not only positrons but also electrons could be injected across the inner boundary from the polar-cap accelerator. If electrons are injected with sufficient Lorentz factor (say,  $10^7$ ), they will not feel  $E_{\parallel}$  near the inner boundary and will return around the point where  $E_{\parallel}$  maximizes. The inward motion of such returned electrons significantly affects the Poisson equation, if their injection rate is a good fraction of the Goldreich-Julian value.

It remains an unsettled issue whether an outer-gap accelerator resides on the field lines on which a polar-cap accelerator exists. To begin with, let us consider the case when the plasma flowing between the polar cap and the outer-gap accelerator is completely charge separated. Such a situation can be realized, for instance, if only positively charged particles are ejected outwardly from the polar cap while there is virtually no electrons ejected inwardly from the outer gap. Neglecting the pair production, current conservation law gives the charge density,  $\rho_e$ , per unit magnetic flux tube as

$$\frac{\rho_e}{B} \propto \frac{j_{\text{tot}}}{v}, \quad (112)$$

where  $v$  refers to the particle velocity along the field line, and  $j_{\text{tot}}$  the conserved current density per magnetic flux tube. At each point along the field line,  $\rho_e$  should match  $\rho_{\text{GJ}}$ . If the field line intersects the null surface,  $\rho_e$  must vanish there; this obviously violates the causality in special relativity. Therefore, a stationary ejection of a completely charge-separated plasma from the polar cap can be realized only along the field lines between the magnetic axis and those intersecting the null surface at the light cylinder. On these grounds, it was argued that an outer-gap accelerator, which is formed close to the last-open field line, may not resides on the same field lines on which an polar-cap accelerator resides. This has been, in fact, the basic idea that an outer gap will not be quenched, because the particles ejected from the polar cap will flow along the different field lines. This idea was welcomed in outer-gap models, because a gap has been considered to be quenched if the external particle injection rate becomes comparable to the Goldreich-Julian value.

In general, however, the plasmas are not completely charge separated and consist of both signs of charge (e.g., positrons and electrons). Such a situation can be realized, for instance, if both charges are ejected outwardly from a polar-cap accelerator, or if positively charged particles are ejected outwardly from the polar cap while electrons are ejected inwardly from the outer gap, or if there is a pair production between the two accelerators. In these cases, the velocities of both charges will be adjusted so that both the current conservation and  $\rho_e = \rho_{\text{GJ}}$  are satisfied at each point along the field lines. Therefore, it seems likely that a polar-cap accelerator and an outer-gap accelerator reside on the same field lines.

To examine if there is a stationary plasma flow

between the polar cap and the outer gap, we must extend the present analysis into the two dimensional momentum space in the sense that the pitch-angle dependence of the particle distribution functions is taken into account. For example, if both charges are ejected from the polar-cap accelerator, electrons will return in the outer gap, screening the original acceleration field in the gap, and violating the original balance of  $\rho_e = \rho_{GJ}$  outside of the gap. Because the returning motion of particles can be treated correctly if we consider the pitch-angle evolution of the distribution functions, and because the pair production is already taken into account, our present method is ideally suited to investigate the plasma flows and  $E_{\parallel}$  distribution self-consistently inside and outside of the gap.

### 6.3. Unification of Outer-gap Models

In addition to the extension into higher dimensions in the momentum space, it is also important to extend the present method into two- or three-dimensional configuration space. In particular, determination of the perpendicular thickness,  $D_{\perp}$ , is important to constrain gap activities. There have been, in fact, some attempts to constrain  $D_{\perp}$  in the CHR picture. Since  $-d\Psi/ds$  is proportional to  $BD_{\perp}^2$ , particles energies, and hence the  $\gamma$ -ray energies increase with increasing  $D_{\perp}$  (for a fixed  $B$ ). Zhang and Cheng (1997) constrained  $D_{\perp}$ , by considering the condition that such  $\gamma$ -rays cause pair production in the gap by photon-photon collisions. Furthermore, Cheng, Ruderman, and Zhang (2000) extended this idea into three-dimensional magnetosphere and discussed phase-resolved  $\gamma$ -ray spectra for the Crab pulsar. In addition to these works, Romani (1996) discussed the evolution of the  $\gamma$ -ray emission efficiency and computed the phase-resolved spectra for the Vela pulsar, by assuming that  $BD_{\perp}^2$  declines as  $r^{-1}$ . However, in these works, screening effects due to pair production has not been considered; thus, the obtained  $D_{\perp}$ , as well as the assumed gap position along the field lines, are still uncertain.

On the other hand, in our approach (picture),  $D_{\perp}$  is not solved but only adjusted so that the  $\gamma$ -ray flux may match the observations. Therefore, the question we must consider next is to solve such geometrical and electrodynamical discrepancies between these two pictures. We can investigate this issue by extending the present method into higher spatial dimensions.

### 6.4. Application to Polar-cap Models

Electrodynamically speaking, the essential difference between outer-gap and polar-cap accelerators is the value of the optical depth for pair production. In an outer-gap accelerator, pair production takes place via  $\gamma\gamma$  collisions and its mean-free path is much greater than the light cylinder radius. Therefore, a pair production cascade takes place gradually in the gap. On the other hand, in a polar-cap accelerator, pair production takes place mainly via magnetic pair production and its mean free path is much less than the star radius for a typical magnetic field strength ( $B \sim 10^{12}$  G, say). Therefore a pair production avalanche takes place in a limited region, which is called as ‘pair formation front’, in the gap (Arons 1981; Harding & Muslimov 1998, 2001, 2002; Shibata, Miyazaki, Takahara 1998, 2002; Harding, Muslimov, Zhang 2002). In an outer magnetosphere, there is a place where the right-hand side of equation (68) vanishes, as long as the injected current density is less than the Goldreich-Julian value. The gap is located around this ‘generalized null surface’, which is explicitly defined in § 2 of Paper VII. Since the sign of  $\rho_e - \rho_{GJ}$  changes at this surface,  $dE_{\parallel}/ds$  changes its sign to be screened out at both the inner and the outer boundaries. On the other hand, there is no ‘generalized null surface’ in the polar cap region. In fact, this surface could be located near to the polar cap surface if  $j^{\text{in}} - j^{\text{out}} \sim 1$  holds; However, such an ‘outer-gap’ like polar-cap accelerator is expected to be less active by the reason described in § 6.1 in Paper VII. Nevertheless,  $E_{\parallel}$  can be instead screened out by the returning particles in the pair formation front in a polar-cap accelerator.

Such a returning motion of particles can be self-consistently solved together with the  $E_{\parallel}$  distribution by our present method, if we implement the magnetic pair production and the resonant IC scattering redistribution functions in the source terms of the particles’ and  $\gamma$ -rays’ Boltzmann equations. We can execute the same advection-phase computation; thus, all we have to do is to add these source terms in the non-advection-phase computation, which is not very difficult. Since analogous boundary conditions (e.g.,  $E_{\parallel} = 0$ ) will be applied, we expect the present method of solving the set of Maxwell and Boltzmann equations is also applicable to a polar-cap accelerator. This is an issue to be examined in our subsequent papers.

One of the authors (K. H.) wishes to express his gratitude to Drs. K. Shibata and A. Figueroa-Vin s for valuable advice on numerical analysis, and to Drs. K. S. Cheng and C. Thompson for fruitful discussion on theoretical aspects. He also thanks Canadian Institute for Theoretical Astrophysics for welcoming him as a visiting researcher.

## REFERENCES

One of the authors (K. H.) wishes to express his gratitude to Drs. K. Shibata and A. Figueroa-Vin  s for valuable advice on numerical analysis, and to Drs. K. S. Cheng and C. Thompson for fruitful discussion on theoretical aspects. He also thanks Canadian Institute for Theoretical Astrophysics for welcoming him as a visiting researcher.

## REFERENCES

Bekenstein, J. D., Oron, E. 1978, Phys. Rev. D, 18, 1809

Beskin, V. S., Istomin, Ya. N., Par'ev, V. I. 1992, Sov. Astron. 36(6), 642

Cha, A. N., Sembach, K. R., Danks, A. C. 1999, ApJ 515, L25

Cheng, K. S., Ho, C., Ruderman, M., 1986a ApJ, 300, 500

Cheng, K. S., Ho, C., Ruderman, M., 1986b ApJ, 300, 522

Cheng, K. S., Ruderman, M., Zhang, L. 2000, ApJ, 537, 964

Chiang, J., Romani, R. W. 1992, ApJ, 400, 629

Chiang, J., Romani, R. W. 1994, ApJ, 436, 754

Combi, J. A., Romero, G. E., Azc  rate 1997, ApSS, 250, 1

Crusius-W  tzel, A. R., Lesch, H. 2002, submitted to Astroparticle Phys.

Daugherty, J. K., Harding, A. K. 1982, ApJ, 252, 337

Daugherty, J. K., Harding, A. K. 1996, ApJ, 458, 278

Harding, A. K., Tademaru, E., Esposito, L. S. 1978, ApJ, 225, 226

Harding, A. K., Muslimov, A. G., 1998, ApJ, 508, 328

Harding, A. K., Muslimov, A. G., 2001, ApJ, 556, 987

Harding, A. K., Muslimov, A. G., 2002, ApJ, 568, 862

Harding, A. K., Muslimov, A. G., B. Zhang, 2002, ApJ, 576, 366

Fierro, J. M., Michelson, P. F., Nolan, P. L., Thompson, D. J., 1998, ApJ 494, 734

Greiveldinger, C., Camerini, U., Fry, W., Markwardt, C. B.,   gelman, H., Safi-Harb, S., Finley, J. P., Tsuruta, S. 1996, ApJ 465, L35

Hirotani, K. 2000a, MNRAS 317, 225 (Paper IV)

Hirotani, K. 2000b, PASJ 52, 645 (Paper VI)

Hirotani, K. 2001, ApJ 549, 495 (Paper V)

Hirotani, K. Okamoto, I., 1998, ApJ, 497, 563

Hirotani, K. Shibata, S., 1999a, MNRAS 308, 54 (Paper I)

Hirotani, K. Shibata, S., 1999b, MNRAS 308, 67 (Paper II)

Hirotani, K. Shibata, S., 1999c, PASJ 51, 683 (Paper III)

Hirotani, K. Shibata, S., 2001, MNRAS 325, 1228 (Paper VII)

Hirotani, K. Shibata, S., 2002, ApJ 558, 216 (Paper VIII)

Hirotani, K. Shibata, S., 2002, ApJ 564, 369 (Paper IX)

Kanbach, G., Arzoumanian, Z., Bertsch, D. L., Brazier, K. T. S., Chiang, J., Fichtel, C. E., Fierro, J. M., Hartman, R. C., et al. 1994, A & A 289, 855

Kaspi, V. M., Lackey, J. R., Manchester, R. N., Bailes, M., Pace, R. 2000, ApJ 528, 445

Koribalski, B., Johnston, S., Weisberg, J. M., Wilson W. 1995, ApJ 441, 756

Krause-Polstorff, J., Michel, F. C. 1985a MNRAS 213, 43

Krause-Polstorff, J., Michel, F. C. 1985b A& A, 144, 72

Manchester, R. N., Mar, D. P., Lyne, A. G., Kaspi, V. M., Johnston, S. 1993, ApJ 403, L29

Mayer-Hasselwander, H. A., Bertsch, D. L., Brazier, T. S., Chiang, J., Fichtel, C. E., Fierro, J. M., Hartman, R. C., Hunter, S. D. 1994, ApJ 421, 276

Michel, F. C., 1991, ApJ, 383, 808

Mignani, R., Caraveo, P. A., Bignami, G. F. 1997, ApJ 474, L51

Moffett, D. A., Hankins, T. H. 1996, ApJ 468, 779

Nel, H. I., De Jager, O. C., Raubenheimer, B. C., Brink, C., Meintjes, P. J., Nortt, A. R. 1993, ApJ 418, 836

Nolan, P. L., Arzoumanian, Z., Bertsch, D. L., Chiang, J., Fichtel, C. E., Fierro, J. M., Hartman, R. C., Hunter, S. D., et al. 1993, ApJ 409, 697

  gelman, H., Finley, J. P., Zimmermann, H. U. 1993, Nature 361, 136

Pavlov, G. G., Zavlin, V. E., Sanwal, D., Burwitz, V., Garmire, G. P. 2001, ApJ, 552, L129

Percival, J. W., et al. 1993, *ApJ* 407, 276

Purnell, D. K. 1975, *Mon. Weather Rev.* 104, 42

Ramanamurthy, P. V., Bertsch, D. L., Dingus, L., Esposito, J. A., Fierro, J. M., Fichtel, C. E., Hunter, S. D., Kanbach, G., et al. 1995, *ApJ* 447, L109

Romani, R. W. 1996, *ApJ*, 470, 469

Romani, R. W., Yadigaroglu, I. A. 1995, *ApJ* 438, 314

Sako, T., Matsubara, Y., Muraki, Y., Ramanamurthy, R. V., Dazeley, S. A., Edwards, P. G., Gunji, S., Hara, T. et al. 2000, *ApJ* 537, 422

Shibata, S. 1995, *MNRAS* 276, 537

Shibata, S., Miyazaki, J., Takahara, F. 1998, *MNRAS* 295, L53

Shibata, S., Miyazaki, J., Takahara, F. 2002, *MNRAS* 336, 233

Smith, I. A., Michel, F. C., Thacker, P. D. 2001, *MNRAS* 232, 209

Sturner, S. J., Dermer, C. D., Michel, F. C. 1995, *ApJ* 445, 736

Takata, J., Shibata, S., Hirotani, K., 2002, in Proc. of University of Tokyo Workshop 2002 on The Universe viewed in Gamma-Rays, eds. Enomoto, R., Mori, M., Yanagita, S., in press.

Takewaki, H., Yabe, T. 1987, *J. Comput. Phys.* 70, 355

Tanaka, R., Nakamura, T., Yabe, T. 2000, *Cpmput. Phys. Commun.* 126, 232

Taylor, J. H., Cordes, J. M. 1993, *ApJ* 411, 674

Taylor, J. H., Manchester, R. N., Lyne, A. G. 1993, *ApJS* 88, 529

Thompson, D. J., Bailes, M., Bertsch, D. L., Esposito, J. A., Fichtel, C. E., Harding, A. K., Hartman, R. C., Hunter, S. D. 1996, *ApJ* 465, 385

Thompson, D. J., Bailes, M., Bertsch, D. L., Cordes, J., D'Amico, N., Esposito, J. A., Finley, J., Hartman, R. C., et al. 1999, *ApJ* 516, 297

van Straten, W., Bailes, M., Kulkarni, S. R., Anderson, S. B., Manchester, R. N., Sarkissian, J. *Nature*, 412, 158

Williamson, D. L., Rasch, P. J. 1989, *Mon. Weather Rev.* 117, 102

Yabe, T., Interface capturing and universal solution of solid, liquid and gas by CIP method, *Proceedings Conf. High-Performance Computing on Multi-phase Flow*, Tokyo, 1997

Yabe, T., Aoki, T. 1991 *Comput. Phys. Commun.*, 66, 219

Yabe, T., Ishikawa, T., Wang, P. Y., Aoki, T., Kadota, Y., Ikeda, F. 1991 *Comput. Phys. Commun.*, 66, 233

Yabe, T., Tanaka, R., Nakamura, T., Xiao, F. 2001, *Mon. Weather Rev.* 129, 332

Yabe, T., Zhang, Y., Xiao, F., A numerical procedure—CIP—to solve all phases of matter together, *Lecture Note in Physics*, Sixteenth Int. Conf. on Numerical Methods in Fluid Dynamics, (Springer-Verlag, New York, 1998), p. 439.

Yabe, T., Xiao, F. 1995, *Nucl. Eng. Design* 155, 45

Zavlin, V. E., Pavlov, G. G., Sanwal, D., Manchester, R. N., Trümper, J., Halpern, J. P., Becker, W 2002, *ApJ* 569, 894

Zhang, L. Cheng, K. S. 1997, *ApJ* 487, 370

Zhang, B., Harding, A. K. 2000, *ApJ* 532, 1150

Zhang, Y., Yabe, T. 1999, *Comput. Fluid Dynamics J.* 8, 378

### A. Reduction of Particle Boltzmann Equations

In this appendix, we derive the Boltzmann equations (18) and (19) from equation (15). To begin with, we consider the momentum derivative terms  $\mathbf{F}_{\text{ext}} \cdot \partial \mathbf{p} N$  in equation (15). Let us describe the momentum vector  $\mathbf{p}$  as

$$\mathbf{p} = p_{\parallel} \mathbf{e}_{\parallel} + p_{\phi} \mathbf{e}_{\phi} + p_{\perp} \mathbf{e}_{\perp}, \quad (\text{A1})$$

where  $(\mathbf{e}_{\parallel}, \mathbf{e}_{\phi}, \mathbf{e}_{\perp})$  forms the orthonormal basis:  $\mathbf{e}_{\parallel}$  and  $\mathbf{e}_{\perp}$  are the unit vectors parallel and perpendicular to the local magnetic field on the poloidal plane, and  $\mathbf{e}_{\phi}$  is the azimuthal unit vector. Defining the angles as in figure A14, we can express the components as

$$\begin{aligned} p_{\parallel} &= p \cos \chi, \\ p_{\phi} &= p \sin \chi \cos \chi_{\perp}, \\ p_{\perp} &= p \sin \chi \sin \chi_{\perp}, \end{aligned} \quad (\text{A2})$$

to obtain

$$\begin{aligned} \frac{\partial}{\partial p_{\parallel}} &= \cos \chi \frac{\partial}{\partial p} - \frac{\sin \chi}{p} \frac{\partial}{\partial \chi}, \\ \frac{\partial}{\partial p_{\phi}} &= \sin \chi \cos \chi_{\perp} \frac{\partial}{\partial p} + \frac{\cos \chi \cos \chi_{\perp}}{p} \frac{\partial}{\partial \chi} \\ &\quad - \frac{\sin \chi_{\perp}}{p \sin \chi} \frac{\partial}{\partial \chi_{\perp}}, \\ \frac{\partial}{\partial p_{\perp}} &= \sin \chi \sin \chi_{\perp} \frac{\partial}{\partial p} + \frac{\cos \chi \sin \chi_{\perp}}{p} \frac{\partial}{\partial \chi} \\ &\quad + \frac{\cos \chi_{\perp}}{p \sin \chi} \frac{\partial}{\partial \chi_{\perp}}. \end{aligned} \quad (\text{A3})$$

Substituting equations (A2) into

$$\mathbf{F}_{\text{ext}} = \pm e \left( -\frac{d\Psi}{ds} \right) \mathbf{e}_{\parallel} - \left( \frac{p_{\parallel}}{p} \mathbf{e}_{\parallel} + \frac{p_{\phi}}{p} \mathbf{e}_{\phi} + \frac{p_{\perp}}{p} \mathbf{e}_{\perp} \right) \frac{P_{\text{SC}}}{c}, \quad (\text{A4})$$

and using equation (A3), we obtain

$$\begin{aligned} \mathbf{F}_{\text{ext}} \cdot \frac{\partial N_{\pm}}{\partial \mathbf{p}} &= \left[ \pm \cos \chi \cdot e \left( -\frac{d\Psi}{ds} \right) - \frac{P_{\text{SC}}}{c} \right] \frac{\partial N_{\pm}}{\partial p} \\ &\mp e \left( -\frac{d\Psi}{ds} \right) \frac{\sin \chi}{p} \frac{\partial N_{\pm}}{\partial \chi}, \end{aligned} \quad (\text{A5})$$

where the plus and the minus signs correspond to the positrons and the electrons, respectively. The result does not depend on  $\chi_{\perp}$ , as expected.

Next, we consider the first and the second terms in equation (15). Since the drift motion due to the

J1059-5237

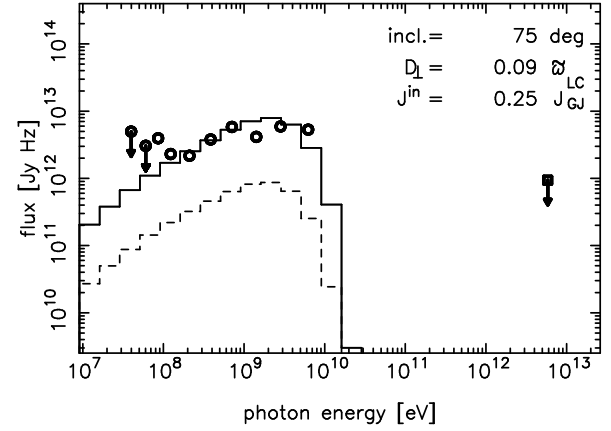


Fig. 13.— Computed  $\gamma$ -ray spectrum for B1055-52. Escaping particles little contribute for the luminosity. The solid and dashed lines correspond to  $d = 0.50$  kpc and  $d = 1.53$  kpc, respectively. Parameters are commonly set as  $D_{\perp} = 0.09 \varpi_{\text{LC}}$ ,  $j^{\text{in}} = 0.25$ ,  $j^{\text{out}} = 0$ .

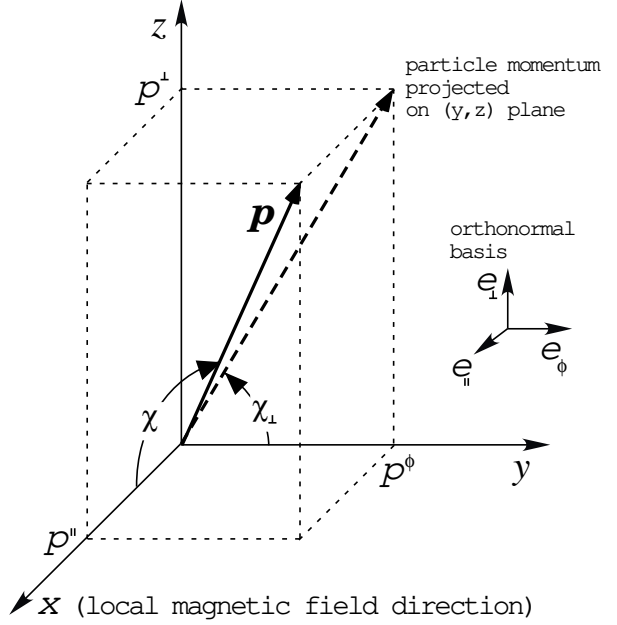


Fig. A14.— Definition of angles in the orthonormal frame  $(\mathbf{e}_{\parallel}, \mathbf{e}_{\phi}, \mathbf{e}_{\perp})$ . The vector  $\mathbf{p}$  represents the three-dimensional particle momentum.

gradient and the curvature of  $\mathbf{B}$  can be neglected in typical outer-gap parameters (Cheng & Zhang 1977), particles exhibit the  $\mathbf{E} \times \mathbf{B}$  drift. Because the deviation of the drift velocity from the corotation,  $\varpi\Omega\mathbf{e}_\phi$ , is of the order of  $O[(B_\phi/B)^2]$ , plasma virtually corotates with the magnetosphere well inside of the light cylinder. Thus, we decouple the toroidal velocity into corotational and non-corotational parts and introduce

$$\tilde{\mathbf{v}} \equiv \mathbf{v} - \varpi\Omega\mathbf{e}_\phi. \quad (\text{A6})$$

Then the first and the second terms become

$$\begin{aligned} \frac{\partial N}{\partial t} + \frac{\mathbf{p}}{m_e\Gamma} \cdot \nabla N &= \frac{\partial N}{\partial t} + \mathbf{v} \cdot \nabla N \\ &= \left( \frac{\partial}{\partial t} + \Omega \frac{\partial}{\partial \phi} \right) N + v_\parallel \frac{\partial N}{\partial s} + v_\perp \frac{\partial N}{\partial z} + \tilde{v}_\phi \frac{1}{\varpi} \frac{\partial N}{\partial \phi} \\ &= \left( \frac{\partial}{\partial t} + \Omega \frac{\partial}{\partial \phi} \right) N + c \left( \cos \chi \frac{\partial N}{\partial s} + \sin \chi \sin \chi_\perp \frac{\partial N}{\partial z} \right) \\ &\quad + \tilde{v}_\phi \frac{1}{\varpi} \frac{\partial N}{\partial \phi}, \end{aligned} \quad (\text{A7})$$

where  $|v_\parallel \mathbf{e}_\parallel + v_\perp \mathbf{e}_\perp| = c$  is used in the last equality. In general, we have to solve this equation, regarding  $\chi$  and  $\chi_\perp$  as independent variables.

It is worth noting that the  $z$  and  $\phi$  derivatives in equation (A7) denote the advection of  $N$  in the trans-field directions. In the present paper, however, we are interested in only  $s$  dependence in the configuration space. Thus, we further reduce the right-hand side of equation (A7), by utilizing the fact that particles are frozen-in. Assuming a stationary magnetosphere as represented in equation (17), and integrating equation (A7) over the momentum space, we obtain

$$\begin{aligned} \int \left[ \frac{\partial N}{\partial t} + \mathbf{v} \cdot \nabla N \right] d^3\mathbf{p} \\ = \int \left( \mathbf{v}_p \cdot \nabla N + \tilde{v}_\phi \frac{1}{\varpi} \frac{\partial N}{\partial \phi} \right) d^3\mathbf{p}, \end{aligned} \quad (\text{A8})$$

where  $\mathbf{v}_p \equiv v_\parallel \mathbf{e}_\parallel + v_\perp \mathbf{e}_\perp$ .

Let us introduce the averaged particle velocity such that

$$\langle \mathbf{v}_p \rangle \equiv \frac{\int \mathbf{v}_p N d^3\mathbf{p}}{\int N d^3\mathbf{p}}, \quad \langle \tilde{v}_\phi \rangle \equiv \frac{\int \tilde{v}_\phi N d^3\mathbf{p}}{\int N d^3\mathbf{p}}. \quad (\text{A9})$$

Then noting (Bekenstein & Oron 1978)

$$\langle \mathbf{v}_p \rangle = \pm \frac{|\langle \mathbf{v}_p \rangle|}{B_p} \mathbf{B}_p, \quad \langle \tilde{v}_\phi \rangle = \pm \frac{|\langle \mathbf{v}_p \rangle|}{B_p} B_\phi, \quad (\text{A10})$$

where plus (or minus) sign is chosen for outwardly (or inwardly) propagating particles, we obtain

$$\int \left[ \frac{\partial N}{\partial t} + \mathbf{v} \cdot \nabla N \right] d^3\mathbf{p} = \pm c \mathbf{B} \cdot \nabla \left[ \frac{1}{B_p} \int N d^3\mathbf{p} \right], \quad (\text{A11})$$

where  $\nabla \cdot \mathbf{B} = 0$  is used. We can neglect the azimuthal derivative in equation (A11), if the azimuthal thickness is large compared with those on the poloidal plane, or if  $B_\phi$  is small compared with  $B_p$ . Under these assumptions, equation (A11) reduces to

$$\int \left[ \frac{\partial N}{\partial t} + \mathbf{v} \cdot \nabla N \right] d^3\mathbf{p} = \int \left[ \pm c B_p \frac{\partial}{\partial s} \left( \frac{N}{B_p} \right) \right] d^3\mathbf{p} \quad (\text{A12})$$

On these grounds, we neglect  $z$  and  $\phi$  dependence of the distribution functions and approximate equation (A7) as

$$\frac{\partial N}{\partial t} + \mathbf{v} \cdot \nabla N = \pm c B_p \frac{\partial}{\partial s} \left( \frac{N}{B_p} \right) \quad (\text{A13})$$

Combining equations (A5) and (A13), and denoting  $N_+$  (or  $N_-$ ) as positronic (or electronic) distribution function, we finally obtain

$$\begin{aligned} \pm c B_p \frac{\partial}{\partial s} \left( \frac{N_\pm}{B_p} \right) + \left[ \pm \cos \chi \cdot \mathbf{e} \left( -\frac{d\Psi}{ds} \right) - \frac{P_{\text{SC}}}{c} \right] \frac{\partial N_\pm}{\partial p} \\ \mp e \left( -\frac{d\Psi}{ds} \right) \frac{\sin \chi}{p} \frac{\partial N_\pm}{\partial \chi} = S(s, p, \chi), \end{aligned} \quad (\text{A14})$$

where  $S$  refers to the source term averaged in a gyration. This equation correctly describes the advection of  $N_\pm$  in the three-dimensional phase space  $(s, p, \chi)$ . If we neglect  $\chi$  dependence (by adopting the mono-pitch-angle assumption), we obtain equation (18) and (19), where  $p = m_e c \sqrt{\Gamma^2 - 1} \approx m_e c \Gamma$  is used.

## B. Inverse-Compton Scattering Redistribution Function

In this appendix, we derive the redistribution function for the IC scatterings. The number of photons upscattered by a single positron or electron into the energy interval  $E_\gamma^*$  and  $E_\gamma^* + dE_\gamma^*$  in time interval  $dt^*$  in the solid angle  $d\Omega_\gamma^*(\theta_\gamma^*, \phi_\gamma^*)$  is given by

$$dN_\gamma = dt^* \int dE_s^* \frac{dF_s^*}{dE_s^*} \int \int \frac{d\sigma_{\text{KN}}^*}{dE_\gamma^* d\Omega_\gamma^*} dE_\gamma^* d\Omega_\gamma^*, \quad (\text{B1})$$

where the asterisk denotes that the quantity is measured in the positron (or electron) rest frame. The

incident photon flux per unit incident photon energy [photons  $\text{s}^{-1}\text{cm}^{-2}\text{erg}^{-1}$ ] is given by

$$\frac{dF_s^*}{dE_s^*} \equiv \frac{1}{E_s^*} \int I_s^*(E_s^*, \Omega_s^*) \cos \Theta^* d\Omega_s^*, \quad (\text{B2})$$

where  $I_s^*$  [ergs  $\text{s}^{-1}\text{cm}^{-2}\text{ster}^{-1}\text{erg}^{-1}$ ] is the specific intensity,  $\Theta^*$  the angle between the photon momentum and the normal vector of a plane across which the incident flux is measured (fig. B15).

When the particle is moving with Lorentz factor  $\Gamma = 1/\sqrt{1 - \beta^2}$ , we can relate the particle rest frame quantities (with asterisks) with the observer's frame (without asterisks) as

$$E_s^* = \Gamma(1 - \beta \cos \theta_s) E_s, \quad E_\gamma^* = \Gamma(1 - \beta \cos \theta_\gamma) E_\gamma, \quad (\text{B3})$$

$$d\Omega_s^* = \frac{d\Omega_s}{\Gamma^2(1 - \beta \cos \theta_s)^2}, \quad d\Omega_\gamma^* = \frac{d\Omega_\gamma}{\Gamma^2(1 - \beta \cos \theta_\gamma)^2}, \quad (\text{B4})$$

$$\cos \theta_s^* = \frac{\cos \theta_s - \beta}{1 - \beta \cos \theta_s}, \quad \sin \theta_s^* = \frac{\sin \theta_s}{\Gamma(1 - \beta \cos \theta_s)}, \quad (\text{B5})$$

$$\cos \Theta^* d\Omega_s^* = \frac{\cos \Theta d\Omega_s}{\Gamma^2(1 - \beta \cos \theta_s)^2}. \quad (\text{B6})$$

Moreover, we obtain the following Lorentz invariant,

$$\frac{I_s^*}{E_s^{*3}} = \frac{I_s}{E_s^3}. \quad (\text{B7})$$

In the observer's frame, the soft photon flux [ergs  $\text{s}^{-1}\text{cm}^{-2}\text{erg}^{-1}$ ] is given by

$$\begin{aligned} E_s \frac{dF_s}{dE_s} &= \int I_s(E_s, \Omega_s) \cos \Theta d\Omega_s \\ &= \pi B_s(T) \left( \frac{r_{\text{NS}}}{r} \right)^2, \end{aligned} \quad (\text{B8})$$

where  $B_s$  is the Planck function is defined by equation (32). Since

$$d\Omega^* \cos \Theta^* \frac{I_s^*}{E_s^*} = d\Omega \cos \Theta \frac{I_s}{E_s} \quad (\text{B9})$$

holds for  $r \gg r_{\text{NS}}$ , we obtain

$$\frac{dF_s^*}{dE_s^*} = \frac{dF_s}{dE_s} = \pi \frac{B_s(T)}{E_s} \left( \frac{r_{\text{NS}}}{r} \right)^2, \quad (\text{B10})$$

as long as the blackbody emission comes from the whole surface of the neutron star. If the observed

emission area of the  $i$ th blackbody component is  $A_j 4\pi r_{\text{NS}}^2$ , equation (B10) is modified as

$$\frac{dF_s^*}{dE_s^*} = \pi \left( \frac{r_{\text{NS}}}{r} \right)^2 \frac{1}{E_s} \sum_j A_j B_s(T_j) \quad (\text{B11})$$

The IC redistribution function is defined by

$$\eta_{\text{IC}}^\gamma(\epsilon_\gamma, \Gamma, \mu_s) \equiv \int d\Omega_\gamma \frac{dN_\gamma}{dt d(E_\gamma/m_e c^2) d\Omega_\gamma} [\text{s}^{-1}], \quad (\text{B12})$$

where  $\mu_s \equiv \cos \theta_s$ . Noting that

$$dt dE_\gamma d\Omega_\gamma = \Gamma^2(1 - \beta \cos \theta_\gamma) dt^* dE_\gamma^* d\Omega_\gamma^*, \quad (\text{B13})$$

and assuming that the specific intensity of the incident photons are unidirectional (i.e.,  $\mu_s = \mu_s^0 = \text{constant}$ ), we obtain

$$\begin{aligned} \eta_{\text{IC}}^\gamma(\epsilon_\gamma, \Gamma, \mu_s^0) &= \frac{1 - \beta \mu_s^0}{\Gamma} \int \frac{d\Omega_\gamma^*}{1 + \beta \cos \theta_\gamma^*} \\ &\times \int d\epsilon_s \frac{dF_s}{d\epsilon_s} \frac{d\sigma_{\text{KN}}^*}{d\epsilon_\gamma^* d\Omega_\gamma^*}, \end{aligned} \quad (\text{B14})$$

where

$$\frac{dF_s}{d\epsilon_s} \equiv \frac{2\pi(m_e c^2)^3}{h^3 c^2} \left( \frac{r_{\text{NS}}}{r} \right)^2 \epsilon_s^2 \sum_j \frac{A_j}{\exp(\epsilon_s/\delta_j) - 1}, \quad (\text{B15})$$

$$\delta_j \equiv \frac{kT_j}{m_e c^2}; \quad (\text{B16})$$

$$\epsilon_s \equiv \frac{E_s}{m_e c^2}, \quad \epsilon_\gamma \equiv \frac{E_\gamma}{m_e c^2}. \quad (\text{B17})$$

In the particle rest frame, the Klein-Nishina cross section is given by

$$\begin{aligned} \frac{d\sigma_{\text{KN}}^*}{d\epsilon_\gamma^* d\Omega_\gamma^*} &\equiv \frac{3\sigma_T}{16\pi} \left( \frac{\epsilon_\gamma^*}{\epsilon_s^*} \right)^2 \left( \frac{\epsilon_s^*}{\epsilon_\gamma^*} + \frac{\epsilon_\gamma^*}{\epsilon_s^*} + (x^*)^2 - 1 \right) \\ &\times \delta \left[ \epsilon_\gamma^* - \frac{\epsilon_s^*}{1 + \epsilon_s^*(1 - x^*)} \right], \end{aligned} \quad (\text{B18})$$

where

$$\epsilon_s^* \equiv \frac{E_s^*}{m_e c^2}, \quad \epsilon_\gamma^* \equiv \frac{E_\gamma^*}{m_e c^2}; \quad (\text{B19})$$

the quantity  $x^*$  refers to the angle between the incident and the scattered photon momenta (fig. B16), and can be expressed as

$$x^* = \cos \theta_s^* \cos \theta_\gamma^* + \sin \theta_s^* \sin \theta_\gamma^* \cos \phi_\gamma^*. \quad (\text{B20})$$

We define  $S^*$  to be the plane containing both the incident and scattered photon momenta. Then  $\alpha^*$

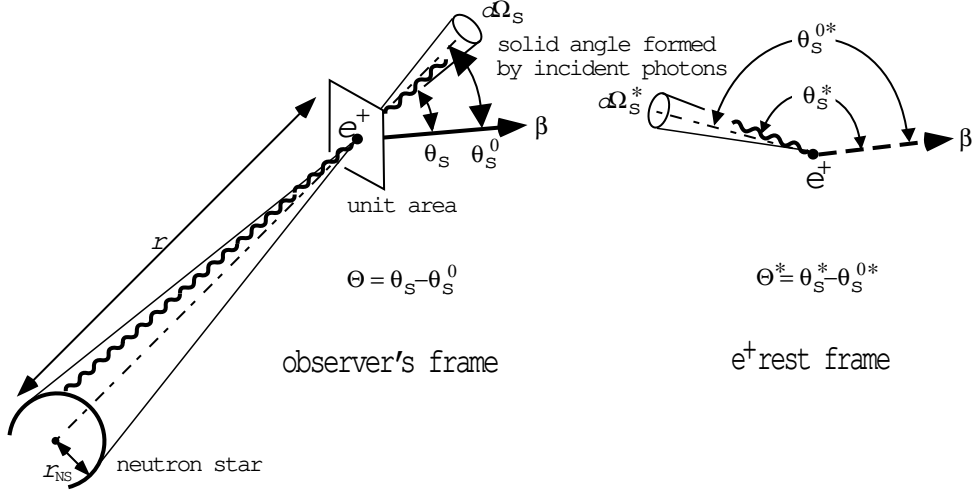


Fig. B15.— Scattering geometry in the observer's frame (non-primed) and the positron rest frame (primed).

means the angle between the normal of  $S^*$  and z axis. Denoting the normal vector as

$$\mathbf{h} = (h_x, h_y, \sqrt{1 - h_x^2 - h_y^2}) \quad (B21)$$

and imposing

$$\begin{aligned} \mathbf{h} \cdot \mathbf{v}_s^* &= h_x \cos \theta_s^* + h_y \sin \theta_s^* = 0, \\ \mathbf{h} \cdot \mathbf{v}_\gamma^* &= h_x \cos \theta_\gamma^* + h_y \sin \theta_\gamma^* \cos \phi_\gamma^* \\ &+ \sqrt{1 - h_x^2 - h_y^2} \sin \theta_\gamma^* \sin \phi_\gamma^* = 0 \end{aligned} \quad (B22)$$

we obtain

$$\cos \alpha^* = \sqrt{1 - h_x^2 - h_y^2} = \frac{f_\Theta}{\sqrt{f_\Theta^2 + \sin^2 \phi_\gamma^*}}, \quad (B23)$$

where

$$f_\Theta \equiv \sin \theta_{sp}^* \cot \theta_\gamma^* - \cos \theta_s^* \cos \phi_\gamma^*. \quad (B24)$$

Solving equation (B20) for  $\cos \phi_\gamma^*$  and eliminating  $\phi_\gamma^*$  from equation (B24), we obtain

$$\cos \phi_\gamma^* = \frac{\theta_\gamma^* - x^* \cos \theta_s^*}{\sin \theta_s^* \sqrt{1 - (x^*)^2}}, \quad (B25)$$

which leads to

$$\begin{aligned} \cos \theta_\gamma^* &= \sin \theta_s^* \sqrt{1 - (x^*)^2} \cos \alpha^* + x^* \cos \theta_s^* \\ &\approx x^* \cos \theta_s^* \quad \text{if } \Gamma \gg 1. \end{aligned} \quad (B26)$$

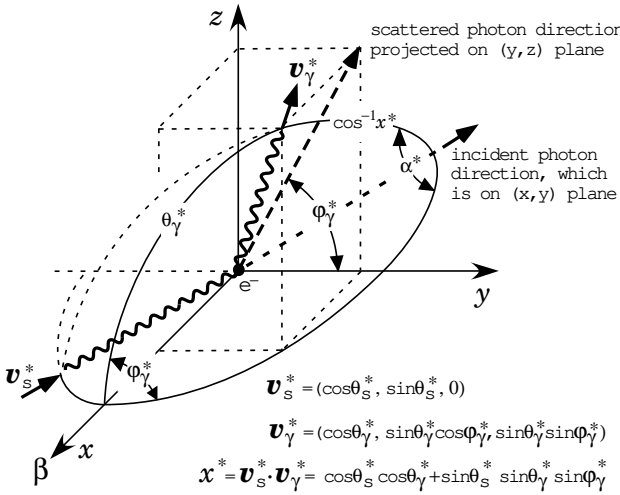


Fig. B16.— Definition of angles in the positron rest frame.

Since

$$d\Omega_\gamma^* = d(-\cos\theta_\gamma^*)d\phi_\gamma^* = dx^*d\alpha^* \quad (\text{B27})$$

holds, we can change the integration variables to obtain

$$\begin{aligned} \eta_{\text{IC}}^\gamma(\epsilon_\gamma, \Gamma, \mu_s^0) &= \frac{1 - \beta\mu_s^0}{\Gamma} \\ &\times \int \frac{dx^*d\alpha^*}{1 + \beta(\sin\theta_s^{0*}\sqrt{1 - (x^*)^2}\cos\alpha^* + x^*\cos\theta_s^{0*})} \\ &\times \int d\epsilon_s \frac{dF_s(\epsilon_s)}{d\epsilon_s} \frac{d\sigma_{\text{KN}}^*}{d\epsilon_\gamma^* d\Omega_\gamma^*}. \end{aligned} \quad (\text{B28})$$

Here,  $\epsilon_s^*$  and  $\epsilon_\gamma^*$  in the right-hand side of equation (B18) should be replaced with  $\epsilon_s$  and  $\epsilon_\gamma$  by equations (B3).

We define the dimensionless IC redistribution function by equation (29). Then, integrating over  $\epsilon_\gamma$  between  $b_{i-1}$  and  $b_i$ , we obtain

$$\begin{aligned} \eta_{\text{IC},i}^\gamma(\Gamma) &= \frac{3\sigma_T}{16\pi\omega_p} (1 - \beta\mu_s^0) \int_{\epsilon_{\min}}^{\epsilon_{\max}} d\epsilon_s \frac{dF_s}{d\epsilon_s} \int_{-1}^1 dx^* \\ &\times \int_0^{2\pi} d\alpha^* f_{\text{IC}}(x^*, \alpha^*, \epsilon_s; \mu_s, \Gamma), \end{aligned} \quad (\text{B29})$$

where  $f_{\text{IC}}$  is defined by equation (34). Substituting  $dF_s/d\epsilon_s$ , and summing up the blackbody components, we obtain equation (33), where  $\mu_s^{0*}$  and  $\mu_s^0$  are denoted as  $\mu_*$  and  $\mu$  in equation (33).